Alexander Pichler

Crystal Structure Solution from Thin Films

Examples of Conjugated Molecules

MASTER THESIS

For obtaining the academic degree
Diplom-Ingenieur

Master Programme of
Technical Physics

Graz University of Technology

Supervisor:

Ao. Univ.-Prof. Dipl.-Ing. Dr. Roland Resel
Institute of Solid State Physics
Graz University of Technology

Graz, May 2013

Deutsche Fassung:
Beschluss der Curricula-Kommission für Bachelor-, Master- und Diplomstudien vom 10.11.2008
Genehmigung des Senates am 1.12.2008

EIDESSTATTLICHE ERKLÄRUNG

Ich erkläre an Eides statt, dass ich die vorliegende Arbeit selbstständig verfasst, andere als die angegebenen Quellen/Hilfsmittel nicht benutzt, und die den benutzten Quellen wörtlich und inhaltlich entnommenen Stellen als solche kenntlich gemacht habe.

Graz, am ……. ……..
(Unterschrift)

Englische Fassung:

STATUTORY DECLARATION

I declare that I have authored this thesis independently, that I have not used other than the declared sources / resources, and that I have explicitly marked all material which has been quoted either literally or by content from the used sources.

……. ……..
date (signature)

Acknowledgement

First I want to thank my supervisor **Roland Resel** who guided me through this year of my master thesis. Roland was always there when I needed support or had questions and he enabled me to go to the synchrotron facility HASYLAB in Hamburg which was an interesting experience. In Hamburg I met the passionate scientist **Ingo Salzmann** who actually provided the beamtime at HASYLAB. It was also a pleasure to meet **Michele Sferrazza** who stayed in Graz for his sabbatical.

I acknowledge the people without whom my work would not have been possible. **Clemens Simbrunner** and **Günther Schwabegger** who prepared NNN thin film samples. **Johannes Gierschner** for the DBDCS samples and **Eric Glowacki**, **Mihai Imria-Vladu** and **Rizwan Ahmed** who manufactured the samples of Tyrian Purple.

I especially thank **Markus Neuschitzer**, who introduced me to the home laboratory setup, the Bruker D8 diffractometer. He spend a lot of his time to show and explain all the important points in order to perform GIXD at the Bruker.

Another big thank goes to **Armin Moser** for the software PyGid which made the data treatment much more convenient. Armin introduced me to the procedure of crystal structure solution from GIXD measurements via simulation.

I had a great time in the "k-Raum" with **Tatjana Duric**, **Alfred Neuhold**, **Michael Dohr**, **Christoph Lercher**, **Michael Zawodski**, **Stefan Pachmajer**, **Michael Pachler** and **Reinhold Hetzel**. Some of them already graduated months ago and others will finish their thesis in the future. The atmosphere was always very supportive and friendly. It was a pleasure to be part of it.

Thank you **Birgit Kunert**, **Elisabeth Stern** and **Harald Kerschbaumer** for providing help for various problems.

Furthermore I want to thank my colleges **Bernhard Nell**, **David Steffelbauer** and **Florian Kolb** who accompanied me from the very beginning of my studies. We learned together, shared lecture scripts and took laboratory exercises. Thank you for your support.

Last but not least I want to thank my father **Friedrich Pichler**, mother **Martha Pichler** and brother **Christopher Lukas Pichler** who always supported me. My family had always faith in me.

Abstract

Organic thin films have interesting electronic and optoelectronic properties and are therefore of high interest in electronics. Organic molecules in thin films often show specific crystal structures which can be different from the known single crystal structures. Such crystal structures are induced by the presence of a surface during the crystallisation process. However, the structural investigation of crystalline thin films is challenging due to the specific crystallographic order and the low scattering volume. Standard X-ray diffraction methods for crystal structure solution cannot be used. This work presents a specific approach to solve crystal structures of thin films. The crystal structure solution is based in a first step on the determination of the crystallographic lattice by indexing the observed Bragg peaks obtained by a grazing incidence X-ray diffraction measurements. In a second step, in order to solve the ubiquitous phase problem of X-ray diffraction, the molecular packing within the crystallographic unit cell is determined by a rigid body simulation of the molecular structure. Thereby possible molecular orientations are sampled in real-space and the respective structure factors are calculated and iteratively optimized against the experimentally obtained structure factors from the Bragg reflections. As a result of the present work the crystal structure of the molecule ternaphthalene grown on thermally oxidized silicon wafers was solved. Furthermore the thin film structure of three different conjugated molecules will be discussed: the well-known dye Tyrian Purple crystallised on polyethylene, copperiodine and siliconoxide surfaces, phenylene-butoxyphenyl-acrylonitrile grown on glass surfaces and dioctylbenzothieno-benzothiophene on thermally oxidised silicon.

Key words: Structure solution, organic thin films, surface-induced crystallization, grazing incidence X-ray diffraction

Kurzfassung

Organische Dünnfilme haben interessante elektronische und optoelektronische Eigenschaften und sind daher im Fokus der Wissenschaft im Feld der Elektronik. Organische Moleküle, die in dünnen Filmen kristallisiert sind, zeigen oft andere Kristallstrukturen, abweichend von der bekannten Einkristallstruktur. Die Bildung solcher Kristallstrukturen ist induziert von der Oberfläche des Substrates während des Kristallisationsprozesses. Die Strukturuntersuchung solcher dünnen Filme ist jedoch eine Herausforderung. Aufgrund der speziellen kristallographischen Ordnung und des kleinen Streuvolumens sind konventionelle Methoden der Strukturaufklärung nicht aufschlussreich. In dieser Arbeit wird eine alternative Methode zur Strukturaufklärung von kristallinen Dünnfilmproben präsentiert. Für die Kristallstrukturlösung ist in einem ersten Schritt die Indizierung der mittels Röntgendiffraktometrie bei streifendem Einfall gemessenen Braggreflexe notwendig. Dadurch wird das kristallographische Gitter ermittelt. Im zweiten Schritt, um das allgegenwärtige Phasenproblem der Röntgenstrukturanalyse zu lösen, wird die molekulare Packung in der kristallographischen Einheitszelle mit starren Molekülen simuliert. Die nach jedem Simulationsschritt erhaltenen Strukturfaktoren werden iterativ auf die experimentell bestimmten Strukturfaktoren optimiert. Als Resultat dieser Arbeit wurde die Kristallstruktur von Ternaphthalen, gewachsen auf thermisch oxidierten Siliziumwafern, gelöst. Zudem wurden im Weiteren die Dünnfilmstrukturen von drei konjugierten Molekülen untersucht: Der bekannte Farbstoff Purpur, kristallisiert auf Polyethylen-, Kupferiodid- und Siliziumdioxidoberfächen, das Molekül Phenylenebutoxyphenyl-Acrylonitrile, gewachsen auf einer Glassoberfläche, und das Molekül Dioktylbenzothienobenzothiophene auf thermisch oxidiertem Silizium.

Schlagwörter: Strukturaufklärung, organische Dünnfilme, oberflächeninduzierte Effekte, Röntgendiffraktometrie bei streifendem Einfall

Contents

Part I

Motivation

Motivation of the work

Organic electronics is a field of high interest. Since recently organic devices made their way to commercial application. Organic light emitting diodes (OLEDs) have a broad use for example in displays for mobile phones. Materials for other devices like organic thin film transistors (OTFTs) or organic solar cells are now in the focus of science. But why are organic materials of interest for electronics? First of all such materials are solution processable which should significantly lower production costs and open up new applications. The limitation of rigid inorganic materials falls and e.g. flexible devices can be build. For example flexible displays which are already realized. Furthermore a seminal idea is the development of environmentally sustainable electronic devices out of natural organic materials. In this context even environmentally sustainable transistors were presented[1].

The research on organic semiconductors can be split into two branches: first the study of polymers and their electronic properties and the second field are small organic molecules. Both, polymers and small organic molecules can form crystals. In a recent technological development polymers loose attention since molecules exhibit better ordered structures. This work focusses on small organic molecules since ordered structures are essential for optoelectronic processes in a material and therefore for electronic devices. The crystal structure determines the properties thus knowledge about the molecular arrangement is of vital importance. The point is to determine the molecular packing of organic crystals in order to understand the physical effects.

As in inorganic electronics thin films are used in the fabrication of OLEDs or OTFTs. Various papers prove that organic crystals show polymorphs when prepared as thin film. The influence of the underlying surface leads to so-called surface-induced phases. Such structures are not solvable with standard X-ray analysis. Due to a small scattering volume and their lateral order a new approach has to be applied. Grazing incidence X-ray diffraction (GIXD) enables structure resolution from thin films. In this work a structure resolution strategy via GIXD will be introduced.

Part II

Fundamentals

1 Molecular Packing of Conjugated Molecules

Crystal structure of organic materials is of vital interest since structure determines the intermolecular overlap of electronic wave functions and thus the electrical and optical properties. This chapter relies on the book by Vainshtein, Fridkin and Indenbom[2] and the book of Kitaigorodsky[3].

Conjugated molecular systems have delocalized electrons which result from an overlap of the atomic p-orbitals across covalent bonds resulting in molecular π-orbitals. For organic systems with alternating multiple and single bonds the $2p_z$ wave functions of carbon form such overlaps which bridge single bonds in order to allow the delocalization of π-electrons. Similar to this intra-molecular overlap inter-molecular overlap of π-orbitals of organic molecules results in (semi)conducting organic materials.

1.1 Molecular Conformation

Most of the molecular crystals are of organic nature. The structural unit of organic crystals is the molecule. The conformation of a single organic molecule in a crystal is determined by covalent bonds and the covalent radii of the atoms. The atomic arrangement with lowest molecular energy U_{mol} defines the conformation. U_{mol} is divisible in four sub-categories:

$$U_{mol} = U_{nv} + U_b + U_{ang} + U_{tors}. \tag{1.1}$$

U_{nv} explains the interaction (van der Waals interaction and hydrogen bonds) of atoms of neighbouring molecules, i.e. non-valence bound atoms of the molecule. U_b and U_{ang} describe deviations from the ideal bond lengths and the ideal bonding angle respectively. U_{tors} accounts for the energetic contribution of rotation of the molecule about the single bonds. Not necessarily only one conformation has lowest energy therefore various isomers might be possible.

When it comes to packing, the energies U_{nv}, U_b, U_{ang} and U_{tors} have different magnitudes, e.g. $U_{ang} \ll U_b$. Consequently when molecules get close in crystallization, atoms rather bend away than alter their bonding length[2].

1.2 Molecular Packing

In general, void space in crystals is always unfavourable[4] and therefore the packing is mainly governed by the close-packing principle. The mutual arrangement of the molecules is such that the "bumps" of one molecule fit in the "hollows" of adjacent

molecules[3]. As atoms for the molecular conformation, molecules aim to minimize the lattice energy when packing. In principle van der Waals forces determine a close packing structure of the molecules with minimal lattice energy. The van der Waals forces between two atoms with a distance r can be described by the Lennard-Jones potential

$$U(r) \;=\; \varepsilon \left[\left(\frac{r_0}{r} \right)^{12} \;-\; 2 \left(\frac{r_0}{r} \right)^{6} \right], \tag{1.2}$$

whereas $U(r_0) = -\varepsilon$, so ε is the extremal depth of the potential well at r_0. Both parameters are empiric. U(r) is lightly attractive for $r > r_0$ and strongly repulsive for $r < r_0$. However hydrogen bonds and Coulomb forces also affect the structural arrangement and for full physical understanding thermodynamic effects, which are relevant due to the weakness of the van der Waals interaction, have to be considered too.

Desiraju et al. presented in [8] an empiric approach to predict crystal structures of aromatic hydrocarbons. They investigated 32 hydrocarbons and analysed their structural arrangements. The major motifs they found in their work were stacked structures (sandwich) and glide structures (herringbone) which originate from C$\cdots$C and C$\cdots$H interactions. By assigning parts of the molecular surface as stack-promoting and glide-promoting they were able to find a simple relation for structure prediction. Each atom is represented due to its position by a certain area of the molecule and in a next step they assigned to the molecules glide and stack contributions. By summing up the respective contributions one gets two areas S_{glide} and S_{stack} whereas the ratio S_{glide}/S_{stack} as a function of the total molecular surface $S_M = S_{glide} + S_{stack}$ allows structure prediction for many poly-nuclear aromatic hydrocarbons.

1.2.1 Hydrogen Bonding

In hydrogen bonding a H-atom interacts attractively with an electronegative atom, like N, O or F, and establishes a polar bond. The bond is directional and stronger than the van der Waals force (compare the bonding energies: 1-3 kcal/mol for van der Waals and 3-10 kcal/mol for H-bonding) but much weaker than a covalent bond. Therefore molecules with such groups form mutual arrangements and structures with two- or three-dimensional networks of hydrogen bonds can arise[2] which alter intermolecular distances and angles and therefore trigger different physical behaviour. The hydrogen bond itself is strongly dependent on factors like temperature and pressure. Despite the high energy range of hydrogen bonds, van der Waals forces determine the close packing in organic crystals.

1.2.2 π-Stacking

Organic crystals in general form insulators however packing of certain molecules in stacks can promote an overlap of the molecular π-orbitals and therefore create even one-dimensional conductors. In organic electronics the conducting properties of organic materials are of vital importance. The two classes of materials for organic semiconductors, namely low molecular weight materials and polymers have in common that they have conjugated π-electron systems. An overlap of the molecular π-orbitals enables

conducting properties. In a π-stack or sandwich structure molecules pack face-to-face, increasing the overlap of the π-orbitals and hence decreasing the bandwidth. The typical π-stacking distance between two molecular planes is 3,4Å to 3,6Å[6].

1.2.3 Herringbone Packing

The simplest and very common pattern in which e.g. hydrocarbons arrange is the herringbone motif[8]. The evolution of such a structure is displayed in figure 1.1. Crystals of organic materials are built up by stacking molecular layers, which fulfil the close-packing principle. However, in order to fully explain the herringbone motif Coulomb interactions have be taken into consideration. The directional Coulomb force has a stabilizing effect on the structure[7].

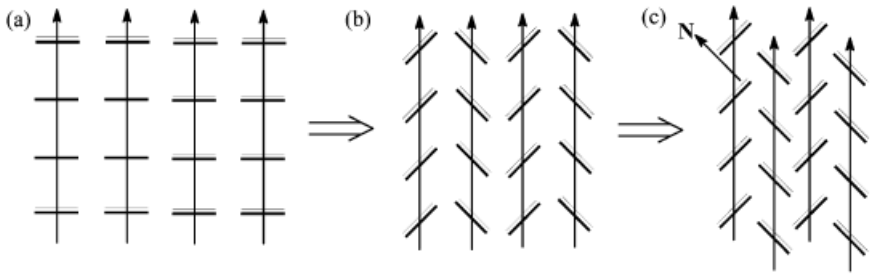

Figure 1.1: Evolution of a herringbone structure. From a cofacial π-stack in picture a the structure develops via rotation (b) and translation (c) to a herringbone. Figure taken from [6].

Monoclinic structures especially $P2_1/c$ play an important role for closest-packed organic crystals. Such structures can be achieved through a monoclinic displacement translation resulting in an arbitrary angle of the layer planes in stacking direction or by inversion centres, by glide planes or screw axes[3]. Such molecular symmetries (e.g. P 2_1 symmetries) promote due to their symmetry operations herringbone packed structures. The molecules in the herringbone structure are packed edge-to-face in a two-dimensional layer (see figure 1.1). This in general minimizes the π-π orbital overlap between adjacent molecules[6]. However, slipped herringbone arrangements, which allow favourable π-π interactions, are observed as well[19].

Theoretically the transport properties of π-stacked molecules should outperform herringbone packed structures however there is no sufficient experimental evidence[6]. This proves that the interplay of transport properties and molecular packing is not fully understood.

1.3 Organic Thin Films

Various examples are known which prove that some organic molecules (e.g. pentacene) exhibit a different structure, not bulk structure, when prepared as thin film. Thermodynamic conditions and crystallization kinetics are very important for crystal growth

and therefore structure. But also the surface on which the material is deposited has an influence on the arrangement of the organic molecules. First for a specific crystal phase the unit cells can arrange with a certain preferred orientation depending on the substrate surface. Moreover the surface, i.e. surface structure and surface contamination, influences the formation of a wetting layer which affects the structure and morphology of the organic thin film[10]. In this context surface-induced polymorphs were discovered[11][12][13][14][15][16][17][18].

As already mentioned crystal structure and molecular orientation is in relation with electronic properties. Consequently such surface induced phases are of high interest due to the fabrication of organic light-emitting diodes (OLEDs), organic thin film transistors (OTFTs) and organic solar cells. The two-dimensional layer structure, typical for organic crystals, enables the directional charge mobility.

In analogy to X-ray powder diffraction, thin films with fibre-texture structure, whereas the fibre axis are perpendicular to the substrate surface, are called two-dimensional powders. The films show well defined structural order in the z-direction but randomly ordered crystallites in the xy-plane like a powder (see figure 1.2).

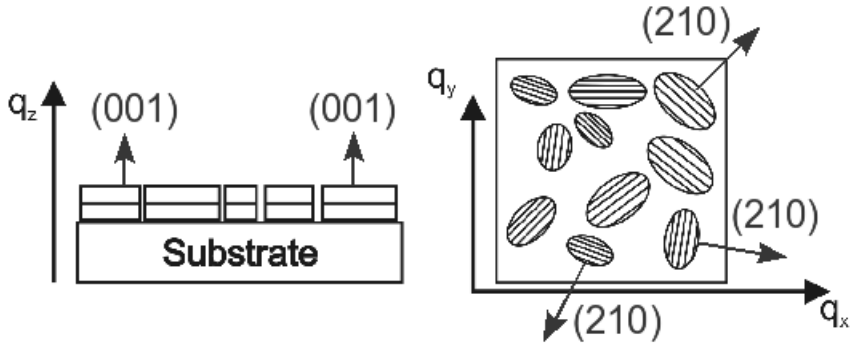

Figure 1.2: Schematic representation of a two-dimensional powder. Figure from [28].

Thin films are often manufactured by adsorption, e.g. from solution, by spin coating, by printing from solution or by with vapour deposition, e.g. hot wall epitaxy or molecular beam deposition[9]. In order to achieve self assembled crystalline structures, the suitable experimental parameter like deposition rate, temperature, etc. have to be found but additionally as stated above the substrate material on which the material is deposited plays an important role.

2 Basic Principles of X-Ray Diffraction (XRD)

This chapter is based on the books of Birkholz[20] and Kittel[21] as well as on the Master thesis[26] of Markus Neuschitzer and the PhD thesis[28] of Armin Moser.

2.1 Crystallography

A crystal is described by its crystal lattice and its respective basis. On each crystal lattice point sits a unit cell which is explained by three basis vectors $\vec{a}$, $\vec{b}$, $\vec{c}$. A common representation for an unit cell are the vector lengths a = $|\vec{a}|$, b = $|\vec{b}|$, and c = $|\vec{c}|$ and the angles between them $\angle\vec{a},\vec{b}{=}\gamma$, $\angle\vec{a},\vec{c}{=}\beta$, $\angle\vec{b},\vec{c}{=}\alpha$. Any point in the crystal lattice can be reached with the vector

$$\vec{r_i} \;=\; n_1\vec{a} + n_2\vec{b} + n_3\vec{c}, \tag{2.1}$$

whereas n_i are integers. Within a unit cell (uc) the atomic positions are described by fractional coordinates ($0 \leq x_f \wedge y_f \wedge z_f < 1$):

$$\vec{r}_{uc} \;=\; x_f\vec{a} + y_f\vec{b} + z_f\vec{c}. \tag{2.2}$$

Therefore an atom with position r_A can be assessed by

$$\vec{r}_A \;=\; \vec{r}_i + \vec{r}_{uc}. \tag{2.3}$$

Directions in the crystal are denoted with [uvw] where u, v, w are the smallest possible integers describing the direction with respect to the basis vectors. Crystal planes are explained by Miller indices (hkl) which are found with following rule:

- Planes can be described by three integers n_1, n_2, n_3 on the the axis $\vec{a}$, $\vec{b}$ and $\vec{c}$.
- The reciprocal values of the numbers are taken and individually multiplied to get all fractions to the least common denominator.

The obtained nominators are the desired Miller indices. In cubic crystals the direction [abc] is always perpendicular to the lattice plane (abc).

2.2 X-ray Scattering

X-ray radiation is due to its wavelength used for crystal structure determination. When impinging X-rays on a crystalline material elastic and inelastic scattering occurs. The

inelastic processes are the Compton and the photoelectric effect which are not regarded for structure determination. In the elastic scattering (Thomson scattering) the electric field of the incoming X-ray photons forces the electrons to oscillate. The electron moves in direction of the oscillating electric field and emits a dipole radiation.

In the kinematic scattering theory those waves interfere and sum up to a measurable diffraction pattern. Multiple scattering events and refraction are neglected. The accessible information of such an experiment is this interference pattern, i.e. the superposition of the scattered waves from the electrons in the sample.

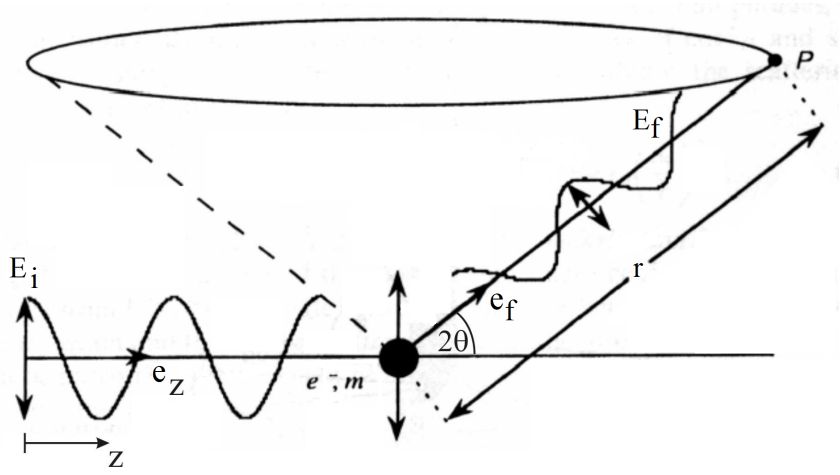

Figure 2.1: Thomson scattering at an electron. The incoming wave E_i travels in z-direction and $\vec{E}_f$ is the scattered field deflected by the angle 2Θ from the incident beam. Figure taken from [22].

In figure 2.1 the incident wave E_i,

$$\vec{E}_i(z,t) \;=\; \vec{E}_0 e^{i(k_0 \vec{e}_z \vec{z} - \omega t)}, \tag{2.4}$$

gets scattered at the electron. ω is the frequency of the wave and $k_0{=}2\pi/\lambda$ is the norm of the wave vector, with λ as wave length. The scattered wave E_f is

$$\vec{E}_f(\vec{r},t) \;=\; \vec{E}_{2\Theta}(\vec{r},t) e^{i(\vec{k}_f \vec{r} - \omega t)} \tag{2.5}$$

in which $\vec{k}{=}2\pi/\lambda \vec{e}_r$ is the corresponding wave vector. Thus the field $\vec{E}_f$ is a function of the angle 2Θ: $E = E(2\Theta)$[1].

De facto in an X-ray experiment not just one single electron oscillates and therefore emits radiation but many do. The resulting scattered planar wave can be written as

$$\vec{E}(\vec{r},t) \;=\; \vec{E}_{2\Theta}(\vec{r},t) e^{i(\vec{k}_f \vec{r} - \omega t)} e^{i\phi}. \tag{2.6}$$

When considering the case of two neighbouring scatterers in a periodic lattice as displayed in figure 2.2 the phase factor $e^{i\phi}$, with $\phi = k_0 \Delta l$, takes the path difference

[1] A beam impinging with angle Θ exits with Θ yielding in an angle between the beams of 2Θ. By convention the scattering angle is described by the angle 2Θ

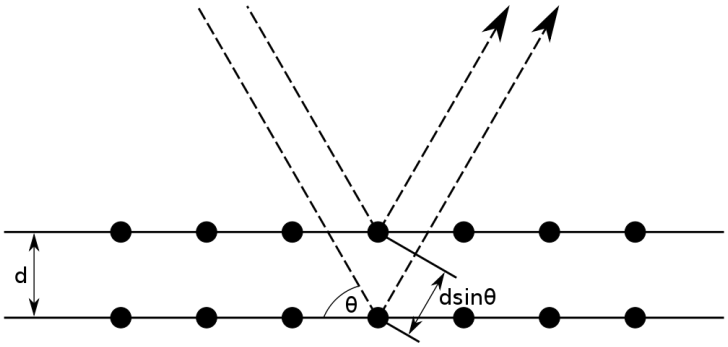

Figure 2.2: Schematic of the Bragg condition. Figure from [23].

of two interfering X-rays into account. From geometrical considerations the length difference of the two beams is

$$\Delta l \;=\; 2d_{hkl}sin(\Theta) \tag{2.7}$$

and the phase ϕ is then

$$\phi \;=\; \frac{2\pi}{\lambda} \cdot 2d_{hkl}sin(\Theta) \tag{2.8}$$

which leads to the **Bragg condition** for constructive interference:

$$2d_{hkl}sin(\Theta) \;=\; n\lambda. \tag{2.9}$$

2.2.1 Ewald Sphere

As explained above, crystals are repetitions of a characteristic unit cell. Each point on this lattice of unit cells is accessed by lattice vectors (equation 2.1). In X-ray diffraction the reciprocal representation is usually more convenient.

In reciprocal space or k-space every point describes a wave and the actual points when transforming a real crystal lattice to k-space are allowed "wave states" of constructive interferences. The reciprocal lattice vectors are (Kittel, p. 34):

$$\vec{a^*} = 2\pi\frac{\vec{b}\times\vec{c}}{\vec{a}\cdot\vec{b}\times\vec{c}},\;\; \vec{b^*} = 2\pi\frac{\vec{a}\times\vec{c}}{\vec{a}\cdot\vec{b}\times\vec{c}},\;\; \vec{c^*} = 2\pi\frac{\vec{a}\times\vec{b}}{\vec{a}\cdot\vec{b}\times\vec{c}}. \tag{2.10}$$

From equation 2.10 it appears that the real and reciprocal lattice vectors are orthonormal. The points of the reciprocal lattice are connected by the reciprocal lattice vector $\vec{G}$,

$$\vec{G} \;=\; h\vec{a^*} + k\vec{b^*} + l\vec{c^*} \quad h,k,l \in \mathbb{Z}. \tag{2.11}$$

The Ewald construction in figure 2.3 links real space with k-space. A X-ray beam with the wave vector $\vec{k_i}$ impinges on the sample. Since we deal here with elastic scattering the exit beam $\vec{k_f}$ has the same length and therefore has to be on the so-called Ewald sphere. If the sphere intersects a point constructive interference for a specific angle 2Θ is created since, as mentioned, the points indicate positive interference. If expressing the contents of figure 2.3 mathematically one obtains:

$$\vec{k_f} \;-\; \vec{k_i} \;=\; \Delta\vec{k} \;=\; \vec{G}. \tag{2.12}$$

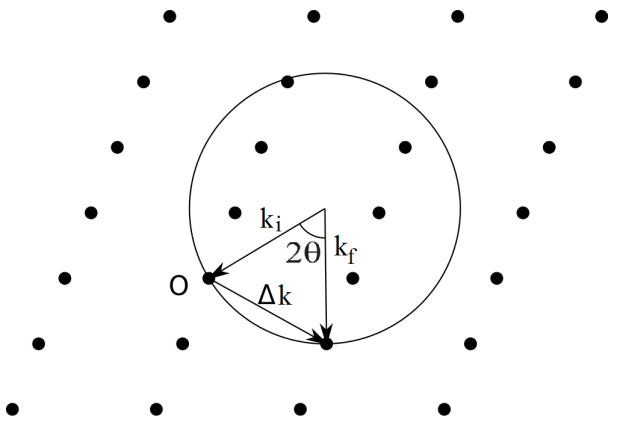

Figure 2.3: The Ewald construction in the reciprocal lattice. Figure from [24].

$\vec{G}$ is a reciprocal lattice vector and the quantity $\Delta\vec{k}$ equates the scattering vector $\vec{q}$. This is the **Laue condition** which is equivalent to Bragg's law in real space written in equation 2.9 (see [21], p. 37).

2.2.2 Structure Factor

In a X-ray diffraction experiment the intensity I of the scattered beam is measured at a detector. I is the squared amplitude of the E-field:

$$I \;=\; E \cdot E^{*}. \tag{2.13}$$

Summation over all participating scatterers (i.e. the fields of the electrons $E_{electron}$) have to be done in order to consider the whole probed crystal. When assuming a large number of scatterers which contribute, the sum can be replaced by a volume integral:

$$\vec{E}(\vec{r}) \;=\; \int_{V} \vec{E_{electron}}(\vec{r}) e^{-i\vec{q}\vec{r}} d\vec{r}. \tag{2.14}$$

As already mentioned the information obtained via X-ray scattering is about the electron density of a crystal. X-rays interact with electrons and in order to derive macroscopic quantities the contributions to scattering of the electrons of one atom have to be summed. The atomic form factor f is a measure of the scattering amplitude of one individual atom,

$$f(\vec{q}) \;=\; \int_{atom} \rho_e(\vec{r}) e^{-i\vec{q}\vec{r}} d\vec{r}. \tag{2.15}$$

This is a Fourier transform of the electron cloud ρ_e of the atom, whereas at $\vec{r} = 0$ is the center of the atom. The resulting atomic E-field is

$$E_{atom}(2\Theta) \;=\; f(\vec{q}) \cdot E_{electron}(2\Theta). \tag{2.16}$$

A crystal might have multiple atoms in the basis. Thus another quantity has to be introduced. Summation over all N atoms of the unit cell with respective atomic form factors f_n gives

$$E_{crystal}(2\Theta) \;=\; \sum_{n=1}^{N} f_n(\vec{q})\; e^{-i\vec{q}\vec{r}_{uc,n}} \cdot E_{electron}(2\Theta), \tag{2.17}$$

with the structure factor F,

$$F \;=\; \sum_{n=1}^{N} f_n \; e^{-i\vec{q}\vec{r}_{uc,n}}. \tag{2.18}$$

The relation between measured intensity and the derived structure factor F is

$$I \;\propto\; F \cdot F^*. \tag{2.19}$$

When calculating the intensity in equation 2.19 it is apparent that the phase factor $e^{-i\vec{q}\vec{r}_{UC}} = e^{i\Phi}$ and therefore information about the positions of the atoms is lost. This is the well-known phase problem of X-Ray diffraction.

2.2.3 The Phase Problem

The phase Φ is not obtained in a diffraction experiment but just by knowing the electronic distribution the crystal structure is fully resolved. Multiple methods were established in order to tackle this issue. The first method was published by Patterson. When dissolving equation 2.19 one gets an expression which is not depended on the atomic position but on the distances between them:

$$|F^2| \;=\; \sum_n \sum_m f_n f_m e^{i\vec{q}(\vec{r_n} - \vec{r_m})} \tag{2.20}$$

The Fourier transform of F is the electron density $\rho_e(\vec{r})$

$$\rho_e(\vec{r}) \;=\; \frac{1}{V} \sum_{h,k,l=-\infty}^{+\infty} F(hkl) e^{-2\pi i(hx+ky+lz)} \tag{2.21}$$

Using this expression and substituting $\vec{r_n}$-$\vec{r_m} = \vec{u}$ = (u,v,w) leads to the Patterson row

$$P(\vec{u}) \;=\; \frac{1}{V} \sum_{h,k,l=-\infty}^{+\infty} |F(hkl)|^2 e^{-2\pi i(hu+kv+lw)} \tag{2.22}$$

and the Patterson function

$$P(\vec{u}) \;=\; \int_V \rho(\vec{r})\rho(\vec{r}+\vec{u}) d\vec{r}. \tag{2.23}$$

The Patterson function has its maxima at the inner-molecular distances and in the coordinate origin at distance zero. Moreover are the intensities proportional to the product of the atomic numbers of the two atoms on the end of the distance vector[29]. The interpretation of the Patterson function is usually difficult and prior knowledge, i.e. an initial guess of the atomic positions, is needed. Heavy atoms like Br or I in the sample facilitate the interpretation because due to the fact that X-rays scatter with electrons X-ray diffraction is not sensitive to light atoms. Additionally there is very little contrast of elements adjacent in the periodic table. On the contrary heavy elements can be clearly distinguished. When dealing with crystals of "equal atoms", i.e. no heavy atoms are present, the initial guess of atomic positions is often not sufficient.

To circumvent this so-called **direct methods** for phase assignment which are based on the relationship between phases and strong reflections were established. Prior knowledge of the system is not necessary. The existence of a relation between symmetry and certain Bragg reflexes allows the prediction of phases and therefore the construction of structure factors. When summing the constructed structure factors the result must yield in a physically valid electron density ρ_e. ρ_e has to be positive and located[30].

Patterson and direct methods are based on the structure factor, a reciprocal quantity. However due to the advances in computer technology the phase problem is also treated vice versa, i.e. from structural arrangements of the atoms or molecules in real space the structure factors are calculated and compared to the measured scattering pattern. Such **direct space methods** optimize the simulated structure and thus the calculated structure factors against the measured quantities in an iteration loop till a satisfying result is found. Depending on the global optimization method such approaches probe a large part of the solution space. Therefore especially for complex structures an educated guess as starting point for the structure optimization is necessary in order to obtain meaningful results. Such methods are widely used in structure refinement like the Rietveld refinement.

2.2.4 Rietveld Refinement

In contrast to the above presented methods the Rietveld refinement is rather a structure refinement method than a structure solution method. Therefore, in order to begin the refinement process a good starting model is needed. Usually, diffraction data is obtained in discrete steps over the scattering angle 2Θ. From the initial model, intensities $y_{c,i}$ for each step i are calculated according to [31]:

$$y_{c,i} \;=\; s\sum_{hkl} L_{hkl}|F_{hkl}|^2\Phi(2\Theta_i - 2\Theta_{hkl})P_{hkl}A \;+\; y_{b,i} \tag{2.24}$$

s is a scale factor,
L_{hkl} contains Lorentz, polarization and multiplicity factors,
F_{hkl} is the calculated structure factor for a specific hkl reflex,
Φ is the reflection profile function,
P_{hkl} is the preferred orientation function,
A is an absorption factor and
$y_{b,i}$ is the background intensity at step i.

The parameters in equation 2.24, which account atomic positions and lattice parameters as well as instrumental geometrical-optical properties and e.g. specimen displacement, etc., are altered to fit the observed intensities y_i. In a least-squares refinement the residual factor S_y,

$$S_y \;=\; \sum_i \frac{1}{y_i}(y_i \;-\; y_{c,i})^2, \tag{2.25}$$

is minimized. Theoretically a perfect result is found when $S_y = 0$ which is practically not achievable.

For structure refinement the adjustable parameters split in global parameters like zero shift of the scattering angle, instrumental profile, profile asymmetry, background intensity, specimen displacement and transparency, wavelength, absorption factor and factors for each phase like the atomic positions, the scale factor, specimen profile, lattice parameters, extinction and preferred orientation (see the book [31] for more information). The Rietveld method is also a powerful tool for quantitative phase analysis, i.e. the determination of the ratio between different phases. In this context a phase is a polymorph of a crystal which might be present in a powder sample.

2.2.5 Structure Validation

The quality of an obtained solution can be judged by residual factors which were introduced for crystal structure refinement. The so-called "R-factors" should be as small as possible for good structure solutions. The three most common factors as presented in [32] are first the unweighted R-factor

$$R \;=\; \frac{\sum ||F_0| \;-\; |F_c||}{\sum |F_0|} \tag{2.26}$$

and second the weighted R-factor

$$wR \;=\; \sqrt{\frac{\sum_i w_i (F_{0,i}^2 \;-\; F_{c,i}^2)^2}{\sum_i w_i F_{0,i}^2}}. \tag{2.27}$$

F_0 are the measured and F_c the respective calculated structure factors. The assessed weight w takes individual uncertainties of the measured reflections into account. For a powder diffraction experiment a structure result with a $R < 5\%$ is good, for R values between 5% - 8% the solution is average and structures with $R > 10\%$ are not good. The third factor is the goodness of fit:

$$GoF \;=\; \sqrt{\frac{\sum w(F_0^2 - F_c^2)^2}{N_R - N_P}}. \tag{2.28}$$

The value N_R is the number of reflections and N_P is the number of refined parameters. In theory when adjusting the weights w the GoF-value should approach 1. However one can also artificially improve GoF by manipulating the weights w.

3 The Experiment

Task of this work is the characterization of crystalline thin films. As already stated in section 1.3 thin films arrange in defined layers of randomly arranged crystallites which represent a 2-D powder. To investigate such samples, techniques and software for single crystals or 3-D powders can be applied. A powerful technique to probe thin films and investigate their crystalline properties is diffraction under grazing incidence.

3.1 Experimental Techniques

3.1.1 Specular Diffraction

In a specular or $\Theta/2\Theta$ measurement in most cases a 3-D powder of randomly distributed crystallite grains is illuminated with monochromatic X-rays. The incident $\vec{k_i}$ and scattered $\vec{k_f}$ wave vector of the X-ray beam sum to the scattering vector $\vec{q}$. All vectors $\vec{k_i}$, $\vec{k_f}$ and $\vec{q}$ are coplanar and $\vec{q}$ has to be parallel to the substrate surface normal $\vec{n}_{hkl}$ in order to satisfy the Laue condition. Thus in a specular scan just information of distances between horizontal planes is obtained. In the case of 3-D powder samples where randomly distributed crystallites contribute to scattering some crystallites fulfil the scattering condition for a specific 2Θ angle and lead to an intensity at the detector. Each hkl Bragg reflex is assigned to a certain distance d_{hkl} in the crystal. With this information unit cell and symmetry can be determined. For resolving the whole structure the intensities of the peaks have to be considered. For layered thin films the out-of-plane layer distances are accessible so e.g. if cubic unit cells arrange with [001] direction on the substrate, reflexes for the {00l} Bragg plane are observed.

3.1.2 Rocking Curve

In a rocking curve measurement the 2Θ angle is kept constant therefore a specific d_{hkl} is fixed and just the sample is tilted that the surface normal $\vec{n}_{hkl}$ is not parallel to $\vec{q}$ however $\vec{k_i}$, $\vec{k_f}$ and $\vec{q}$ are coplanar. Consequently the specular condition is just complied when the crystallites are not perfectly aligned. With aid of such measurements the mosaicity of single crystals can be examined or in the case of 3-D powder samples the resolution function of the equipment is obtained. In the case of 2-D powders one can check how well defined the preferred orientation in out-of-plane direction is. To summarize a rocking curve maps the orientation distribution of the crystallites in a powder sample. The wider the curve the lower defined is the preferred orientation and therefore the lower the quality of the sample regarding crystallinity.

3.1.3 Grazing Incidence X-Ray Diffraction (GIXD)

The GIXD geometry combines the Bragg condition and the condition for total external reflection of X-rays from crystal surfaces[25]. This makes the technique extremely surface sensitive (compare ≈10nm for GIXD to up to 1mm for specular scans of organic materials). Moreover an evanescent wave field is established on the surface which enhances the scattered wave up to a factor of two at $\alpha_i = \alpha_c$. The reason for this is that incident, reflected, and transmitted wave fields couple coherently at the surface[26]. By scattering with the evanescent wave the in-plane structure is resolved as displayed in figure 3.1 where the probed lateral Bragg planes are indicated. Consequently this technique is perfectly suited to investigate crystalline thin films.

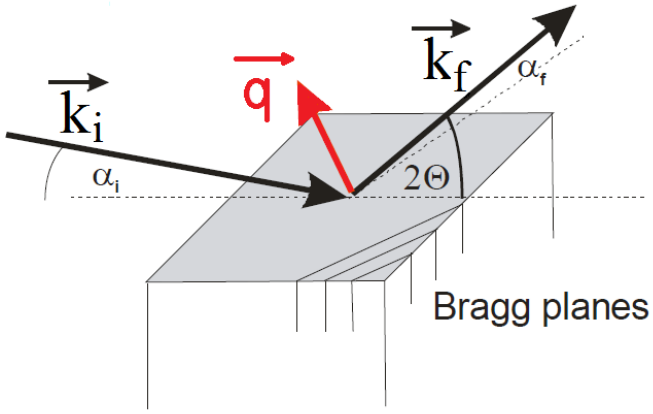

Figure 3.1: Simple representation of the GIXD geometry. The wave vectors of the incident wave $\vec{k}_i$ and the scattered wave $\vec{k}_f$ sum to the momentum transfer $\vec{q}$. Picture from [39].

The measured result is a so-called reciprocal space map of the in-plane and out-of-plane components, $q_p = \sqrt{q_x^2 + q_y^2}$ and q_z respectively, of the momentum transfer $\vec{q}$.

Index of Refraction for X-Rays

The index of refraction n in the X-ray region consists of additional terms, dispersion δ and absorption β, which lead to

$$n = 1 - \delta + i\beta. \tag{3.1}$$

For X-rays δ is of the magnitude of $\approx 10^{-6}$ and always positive. Therefore n is smaller than one which results in total external reflection under a certain critical angle α_c. By applying Snell's law

$$n_{air} \cdot sin(\frac{\pi}{2} - \alpha) = n \cdot sin(\frac{\pi}{2} - \alpha_t), \tag{3.2}$$

with $n_{air} = 1$ and the angle $\alpha_t = 0$ of the transmitted wave due to total reflection, one gets

$$cos(\alpha_c) = n \tag{3.3}$$

and finally for α_c

$$\alpha_c = \sqrt{2\delta}, \tag{3.4}$$

when assuming that the absorption $\beta = 0$ and cos(x) ≈ (1 - $x^2/2$) for x ≈ 0 according to Birkholz (p. 162). The dispersion term δ is rooted in electrons which can be treated as ensemble of damped harmonic oscillators oscillating the X-ray field (Birkholz, p. 160):

$$\delta = \frac{-\rho_e}{2\pi m_e} \frac{e^2}{4\pi\epsilon_0} \sum_i \frac{s_i}{\nu_i^2 - \nu^2}. \tag{3.5}$$

Thereby it can be assumed that the exiting frequency exceeds the resonance frequency of the solid by far, $\nu \gg \nu_i$, and the oscillator strengths s are normalized: $\sum s_i$=1. Considering this an other expression for the critical angle can be derived to

$$\alpha_c = \lambda\sqrt{\frac{r_e\rho}{\pi}}. \tag{3.6}$$

The classical radius of an electron r_e is 2,82e10^{-6}nm and the electron density ρ_e can be determined from a known unit cell.

Dynamical Scattering

Under specular conditions ($\alpha_i \gg \alpha_c$) scattering can be sufficiently described with the Born Approximation (BA) of the kinematic scattering theory where refraction and multiple scattering events are neglected. However when impinging a thin film sample under grazing incidence ($\alpha_i \approx \alpha_c$) refraction and multiple scattering events have to be considered[37]. Therefore the formalism of the Distorted Wave Born Approximation (DWBA) is introduced.

Transmitted rays in a film are refracted and have therefore different wave vectors $\vec{k}$ than the initial vacuum or air wave vectors. The vertical component k_{z2} of the wave vector in the film is then

$$k_{z2} = \sqrt{k_{z1}^2 - k_{zc}^2}, \tag{3.7}$$

whereas k_{z1} is the z-component of the incident wave and k_{zc} the wave vector at the critical angle of total external reflection. Figure 3.2 displays all possible scattering events which occur under grazing incidence. The resulting four momentum transfers in z-direction are according to [40]:

$$q_{1z} = k_{z2f} - k_{z2i} \tag{3.8}$$

$$q_{2z} = -k_{z2f} - k_{z2i} \tag{3.9}$$

$$q_{3z} = k_{z2f} + k_{z2i} \tag{3.10}$$

$$q_{4z} = -k_{z2f} + k_{z2i} \tag{3.11}$$

Term 1 has the same result as the Born approximation. The z-parts of the incident wave vector

$$k_{z2i} = k_0 sin\left(acos\left(\frac{n_1 cos(\alpha_i)}{n_2}\right)\right) \tag{3.12}$$

and the exit wave vector

$$k_{z2f} = k_0 sin\left(acos\left(\frac{n_1 cos(\alpha_f)}{n_2}\right)\right) \tag{3.13}$$

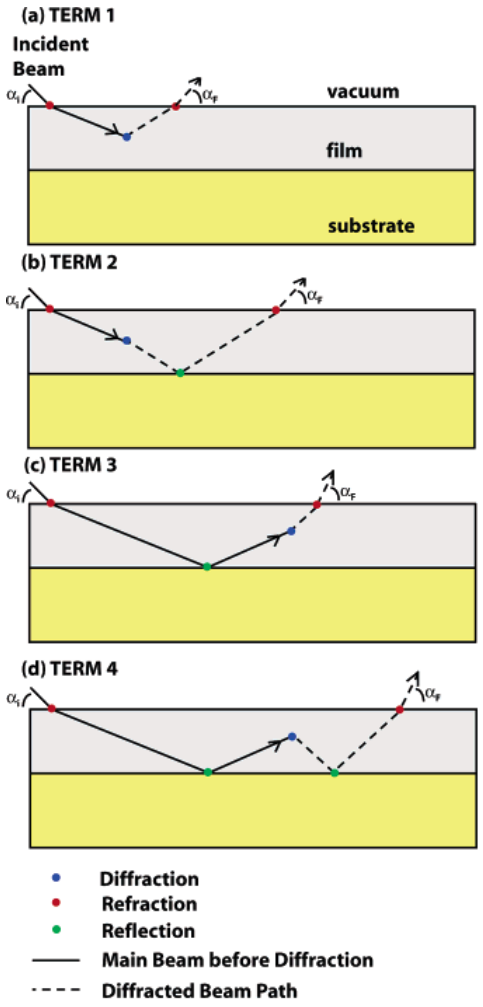

Figure 3.2: This figure illustrates the four different possible scattering events. Diffraction, reflection and refraction are considered. The figure is taken from [40].

complete the description of all scattering events, whereas n_1=1 when impinging from air or vacuum and n_2=cos(α_c) according to Snell's law. The magnitude of the wave vector is k_0=$2\pi/\lambda$. Tate et al. derived expressions for the exit angles α_f for the terms which reveal that terms 1 and 2 are equivalent as well as terms 3 and 4. Thus there are just two cases to distinguish: Diffraction from the transmitted beam and diffraction after reflection from the substrate material.

3.2 Experimental Setup

3.2.1 In-House Equipment

The coplanar experiments were conducted at a PANalytical Empyrean X-ray diffractometer (see figure 3.3). Due to the two circle geometry, i.e. the detector moves on a Θ circle and the X-ray tube on a 2Θ circle, the sample stays always horizontal. A multilayer mirror collimates the diverge X-rays from the X-ray tube. On the detector side a vertical Soller slit reduces the effects of air scattering.

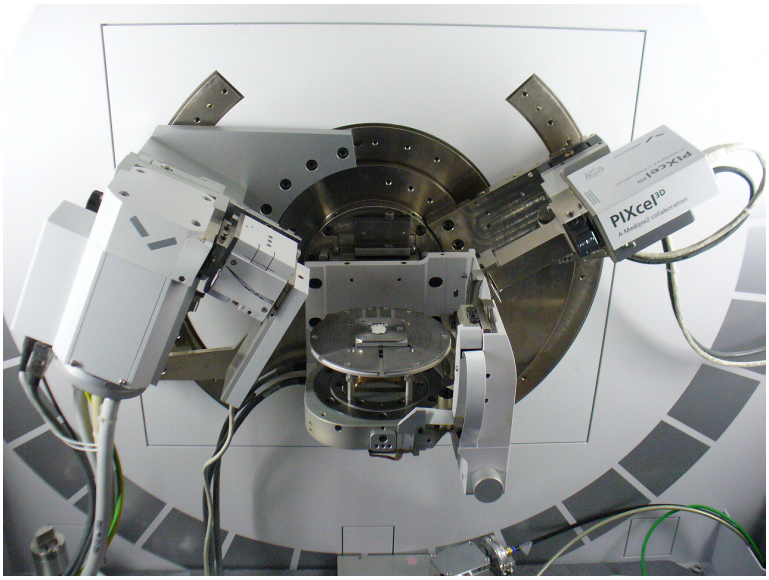

Figure 3.3: Photograph of the PANalytical Empyrean diffractometer setup. X-ray tube with incident beam optics, multilayer mirror for collimation and automatic attenuator, on the left side of the picture, PIXcel detector with Soller slit on the right side and the mounted powder sample in the middle on the sample stage.

Core of the home laboratory setup for GIXD measurments is an adapted Bruker D8 Discover X-ray diffractometer. A schematic representation of the adapted Bruker diffractometer is displayed in figure 3.4. This device is used to pre-characterize thin film samples by GIXD. The incident angle is usually 0,17° for organic films. Neuschitzer et al. demonstrated in [27] the capabilities of this setup by comparing in-house and synchrotron measurements of pentacene monolayers. The data acquisition in q_z-direction is limited due to the out-of-plane range of the PSD Vantec-1 detector of 7,3°. The alignment of the sample is crucial for the experiment. An comprehensive manual can be found in appendix A in [26].

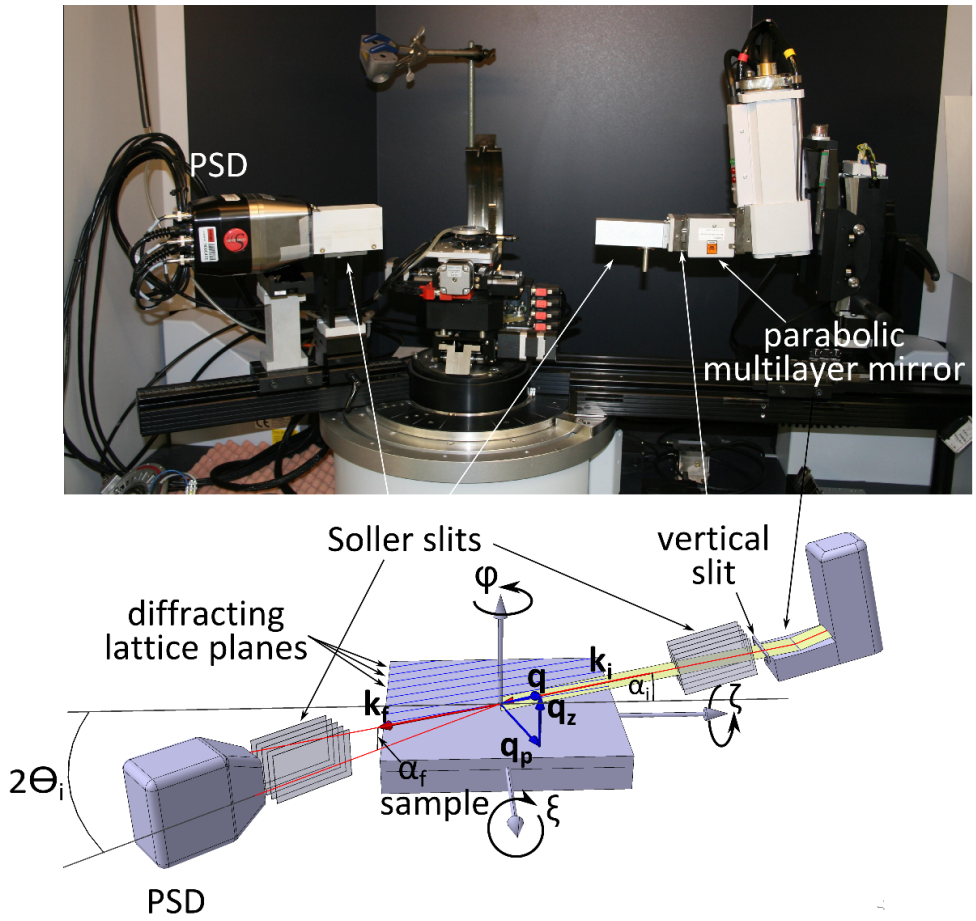

Figure 3.4: Schematic representation of the setup for GIXD experiments in the home laboratory. *The wave vectors of the incident wave and a scattered wave (k_i and k_f, respectively), the corresponding momentum transfer q, and its in-plane and out-of-plane components(q_p and q_z, respectively), as well as the probed lattice planes are indicated.* Figure and italic text taken from [26].

3.2.2 HASYLAB W1 Beamline

The 4,5GeV positron accelerator DORIS III is source of the beamlines of the HASYLAB facility which is part of DESY in Hamburg. The W1 beamline has a 32-pole wiggler as insertion device and a goniometer (figure 3.5) which enables GIXD experiments. The

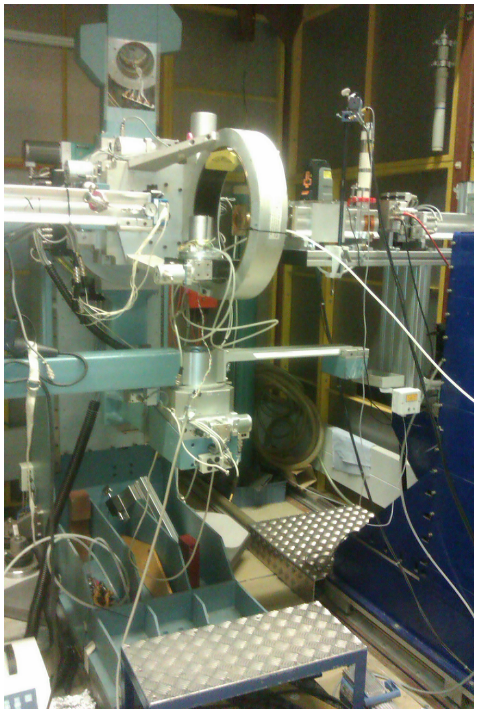

Figure 3.5: Goniometer in the hutch of W1 beamline at HASYLAB. The X-ray beam impinges the sample in the middle of the goniometer from the right.

major drawback of the in-house setup is the data acquisition time. Because of the low beam intensity the measurement of a single reciprocal space map takes about 48 hours at the Bruker D8 whereas at the HASYLAB W1 beamline where the intensity is much higher the time needed is about 20min. Another restriction of the home laboratory setup is that the detector covers a range of approximately 7° starting at q_z=0 and there is no simple way to adjust the detector height to record several reciprocal space maps for different q_z ranges. This limits the collectable amount of data.

In order to determine the wavelength of the beam at HASYLAB a silicon standard was used. Zero channel and resolution of the detector were obtained as well. All values for the two beamtimes are given in table 3.1. All samples apart from the Tyrian Purple

Table 3.1: Parameters for beamline W1 at HASYLAB for the beamtimes in May and September 2012 respectively. The wavelength λ of the X-ray beam, the zero channel c_0 and the resolution cpd (channels per degree) of the detector.

	May 2012	Sept. 2012
λ [Å]	1,1790	1,1802
c_0	639,693	637,320
cpd	331,099	328,221

bulk phase sample (section 6.1) were measured at the first beamtime in May 2012. At the synchrotron the samples were mounted in an Anton Paar DHS 900 stage and probed under helium atmosphere in order to reduce oxidation effects. Sample alignment was done with a standard routine.

3.3 Data Treatment

3.3.1 PyGid

The custom-made software PyGid was used for data treatment and evaluation. PyGid was developed in Python by Armin Moser and is extensively explained and documented in [28]. With the aid of PyGid it is possible to transform the measured data in reciprocal space, to index the obtained reciprocal space maps and extract the intensities of the Bragg peaks. The used tool is the "Integrated line scan" which integrates the measured intensity over a user chosen area in q-space. This area is represented as matrix with intensity entries for discrete q_z and q_p. In this work extracted intensities are always summed along columns yielding in a function $I(q_z)$ for the chosen area. $I(q_z)$ is fitted with a Gaussian and a background is subtracted. The area under the Gaussian is then used as a measure for the intensity. Peak areas are a better measure for the intensity than peak heights because the areas are less susceptible to fluctuations[20] and the peak heights depend on the incident angle of the diffracted beams on the detector whereas the areas of a peaks do not[28].

The intensities are then corrected according to chapter 2.7 in [28] in order to obtain the structure factors. Four correction factors have to be considered: First the Lorentz factor which is a kinematic correction since the integration time differs depending on the angle. The polarization factor regards the polarization of the X-ray source and the appearing 2Θ angle. Third the area factor which accounts the angle-dependent altering of the beam footprint on the sample and finally the rod interception factor which is necessary due to diffuse scattering from the surface. The impact of the four different correction factors is displayed in figure 3.6. A Python script (correct_iobs.py) generates an already FOX-conform input file with the corrected structure factors.

3.3.2 Free Objects for Crystallography (FOX)

FOX is an open source software designed to resolve crystal structures from powder diffraction data[33]. The version used in this work is version 1.9.7.
In order to tackle the phase problem the molecular orientation is sampled in real space and the respective structure factors are calculated and compared to the measured structure factors. In an iterative process the structure solutions are optimized to the measured data. The optimization employs either simulated annealing or a parallel tempering algorithm.

The approach of this work is to solve the crystal structure of 2-D powders instead of usual 3-D powder samples. The major difference for structure resolution is the amount of usable reflections which is much higher for 3-D powders. Moreover the quality of

GIXD data is usually lower. The accuracy of simulation results is therefore not as good as for 3-D powders. A brief manual for the software can be found in the appendix.

3.3.3 Mercury

The evaluation of the obtained molecular arrangements partially happens in the software Mercury which is freely available in a basic version[45]. Crystal structures can be loaded as "Crystallographic Information File" or .cif-files and a 3-D visualisation is generated and further analysis can be performed. In this work all pictures of packed molecules were generated in Mercury.

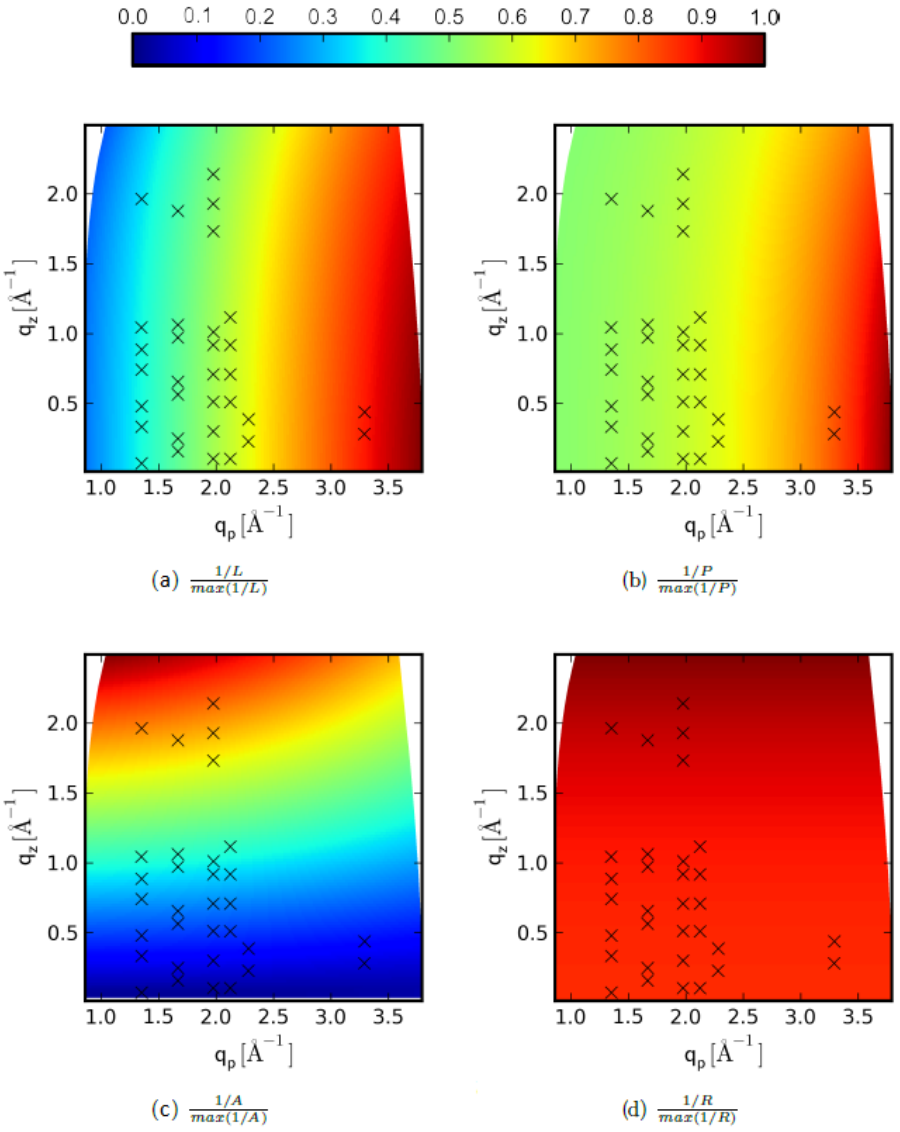

Figure 3.6: Graphical display of the impact of the Lorentz (a), polarization (b), area (c) and the rod interception factor (d) which are normalized to one. This figure is taken from [28].

Part III

Results

4 Dioctylbenzothieno-Benzothiophene (C8-BTBT)

C8-BTBT (structural formular in figure 4.1) enables 2D charge charier transport and is used as active layer in field effect transistors[34]. The molecular packing is already solved by Izawa et al.[35] and displayed in figure 4.2. The obtained structure is monoclinic with P 2_1/a symmetry.
Nevertheless a structure solution was tried in order to check the reliability of the GIXD setup. The sample was manufactured with spin coating from solution on Si-wafers with a 150nm thermally grown SiO_2 layer. The achieved film thickness was approximately 100nm.

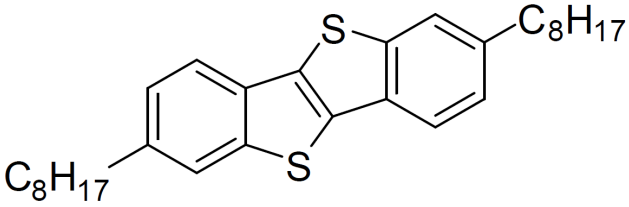

Figure 4.1: Structural formula of Dioctylbenzothieno-Benzothiophene ($C_{30}H_{40}S_2$). Picture taken from [36].

	C_8-BTBT
Empirical formula	$C_{30}H_{40}S_2$
Formula weight	464.77
Crystal color, Habit	colorless, plate
crystal Dimensions/mm^3	$0.50 \times 0.50 \times 0.10$
Crystal system	*monoclinic*
a/Å	5.927(7)
b/Å	7.88(1)
c/Å	29.18(4)
β/°	92.443(4)
V/Å^3	1362(3)
Space group	$P2_1/a$
Z value	2
Temperature	293 K
No. of reflections measured	2743
No. of reflections	1268
No. of variables	145
Residuals: R; wR^2	0.070; 0.152
Goodness-of-fit indicator	1.329

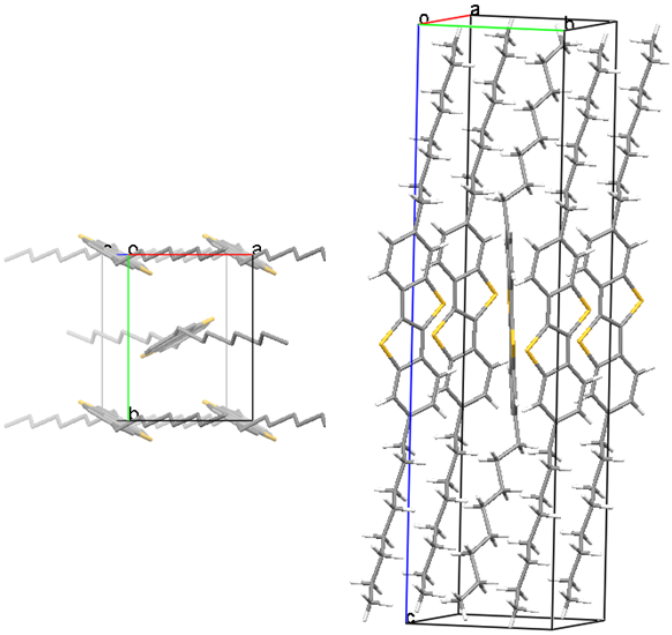

Figure 4.2: The solved single crystal structure parameters on the left and the actual molecular packing on the right. Figure taken from [35].

4.1 Indexation

A GIXD measurement was performed at the HASYLAB facility. The measurement was recorded with an incident angle α_i of 0,15° in a 2Θ-range of 7° to 30°. The step size $\Delta 2\Theta$ was 0,05° with 2s integration time. The obtained reciprocal space map in figure 4.3 shows a thin film with mosaicity. An indexation of the unit cell parameters was possible and the found monoclinic unit cell in table 4.1 fits the measured Bragg peaks and is furthermore in good accordance to the already published solution by Izawa. However due to the blurred Bragg peaks intensity extraction is not feasible and thus structure solution not possible.

Table 4.1: Comparison of the found indexation with already published unit cell values.

	This work	[35]	Differences
a [Å]	5,887	5,927	0,040
b [Å]	7,909	7,880	0,029
c [Å]	28,860	29,180	0,32
β	91,900°	92,443°	0,543°

4.2 Conclusion

C8-BTBT was used as test case to check the reliability of the applied GIXD structure solution approach. The poor quality of the thin film sample does not permit the intensity extraction. The reason for the high mosaicity might be the fabrication via spin coating where the obtained crystal structures are not well ordered. Usually vapour deposited films have better aligned crystallites and therefore lower mosaicity. Nevertheless unit cell parameters of the crystal structure were found which are in good accordance to the literature values.

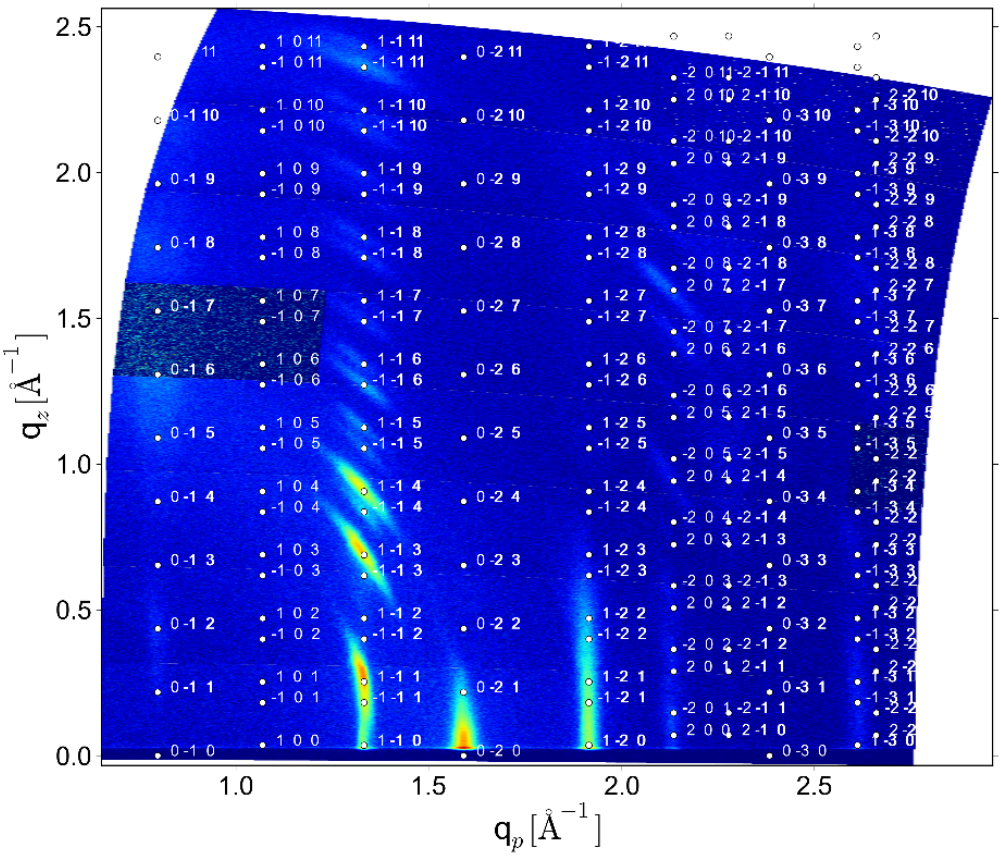

Figure 4.3: Indexed GIXD measurement of C8-BTBT. Blurred peaks are usually an indicator for high mosaicity. The contact plane of the molecules on the SiO_2 surface is the (0 0 1) plane.

5 Ternaphtalene (NNN)

The molecule Ternaphtalene (abbreviated with NNN due to the three connected Naphtalene units) in figure 5.1 has the chemical formular $C_{30}H_{20}$.

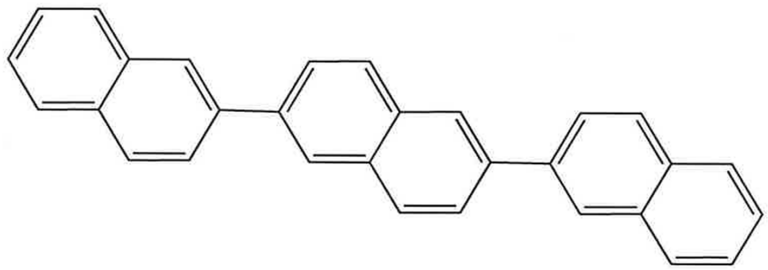

Figure 5.1: Schematic structure of NNN

NNN is a conjugated molecule with optoelectronic properties. Thin films of NNN are for example used for blue and infra-red emitting OLEDs. The NNN powder was synthesized by Theo Dingemans at the Delft University, Netherlands and the thin film samples from the powder were prepared by Clemens Simbrunner and Günther Schwabegger from the JKU Linz. The film was deposited with hot wall epitaxy (HWE) on a silicon-dioxide (SiO_2) surface with a film thickness of about 800nm. The details of the preparation are listed in table 5.1. Additionally a sample with a NNN film on highly ordered pyrolytic graphite (HOPG) was prepared and is discussed at the end of this chapter.

Table 5.1: Relevant details of the sample preparation in the HWE chamber.

Source temperature	150°C
Wall temperature	170°C
Substrate temperature	80°C
Pre-heating time	30min
Deposition time	210min
Deposition rate	≈4nm/min

In order to get a first impression of the surface of the NNN-on-SiO_2 sample, atomic force microscopy (AFM) was applied. Due to the terrace structure in figure 5.2 standing molecules with a contact plane (0 0 1) are assumed.
All necessary steps for the structure resolution from a thin film sample are presented in this chapter. The strategy is as stated in [28]:

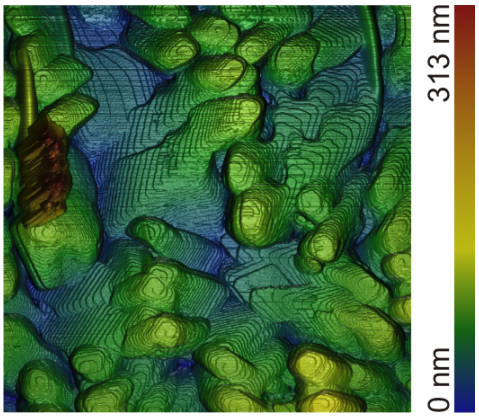

Figure 5.2: The AFM measurement ($10\mu m \times 10\mu m$) of NNN on SiO_2 shows terrace-like structures. This is an indicator for molecules which are standing upright on the substrate, i.e. the molecular backbone is upright standing to the surface.

1. Specular and GIXD measurements
2. Indexation in order to find a unit cell for the investigated structure: Starting from an educated guess the Bragg reflections are iteratively indexed in PyGid.
3. Extraction of the intensities from the reciprocal space map: The area around the peak in the reciprocal space map is integrated in PyGid. The area beyond the obtained 2-dimensional curve corresponds to the intensity of a Bragg reflection.
4. Calculation of structure factors by applying the correction factors to the intensities, namely area, polarisation, Lorentz and rod-interception factor.
5. Structure optimization against extracted structure factors in FOX using rigid body refinement.
6. Evaluation of the obtained structure against the measured pattern
7. If necessary introduction of additional information for the optimization procedure, such as fixing positions of molecules or anti-bump constraints.
8. Rerun of steps 4 to 6 until a satisfactory solution is found or none seems feasible.

In the next step a standard specular scan of the sample was performed. This gives information about the out-of-plane distances, i.e. in z-direction. From the measurement in figure 5.3 for NNN on SiO_2 the distance between the lattice planes was determined to 19,590Å for K_α radiation and 19,593Å for K_β radiation. Those values are average values whereas the peaks at low 2Θ-values were neglected since for low angles the effects of misalignment carry more weight.

5.1 GIXD measurement

A first GIXD measurement was taken at the adapted Bruker D8 diffractometer (see chapter 3.2.1). The data was recorded between $2\Theta = 5°$ - $39°$, with a step size $\Delta 2\Theta$

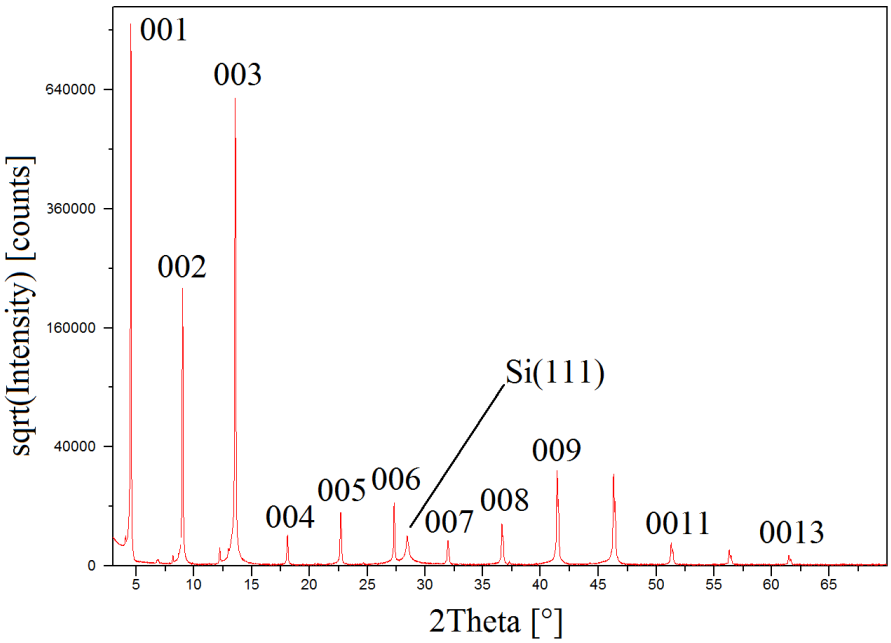

Figure 5.3: Specular scan of NNN on SiO_2 with indexed Bragg reflections up to 13th order. The peaks originate from K_α radiation and a silicon peak is also visible.

= 0,05° and an integration time of 240s. The reciprocal space map in figure 5.4 shows well defined features which indicate a high crystallinity of the film. This data however is not sufficient for a reliable structure resolution. Consequently the NNN thin film sample is just precharacterized in the home laboratory in order to see if the film is worthwhile to be further analysed, which is the case here, and to define a q_p region of interest.

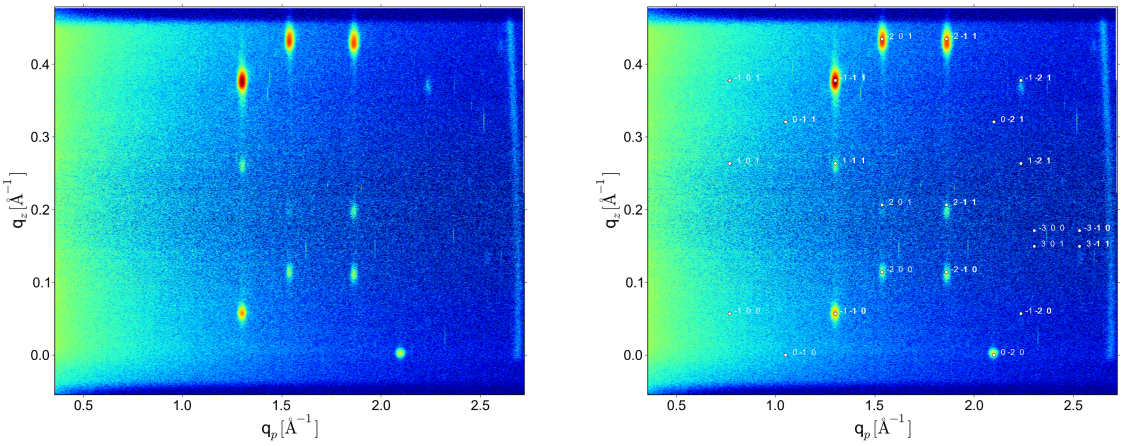

Figure 5.4: Home laboratory GIXD measurement of NNN. Figure with indexation on the right. Respective values for the unit cell can be found in table 5.2.

The measurement depicted in figure 5.4 took about 48 hours. In order to get more comprehensive data in reasonable time measurements are performed at synchrotrons.

5.1.1 Peak splitting phenomena

The first measurement of NNN at HASYLAB in figure 5.5 showed split Bragg peaks. The parameters for the data acquisition were: incident angle $\alpha_i = 0{,}15°$, 2Θ-range = 2° - 35°, step $\Delta 2\Theta = 0{,}01°$ with an integration time of 2s. In order to further investigate

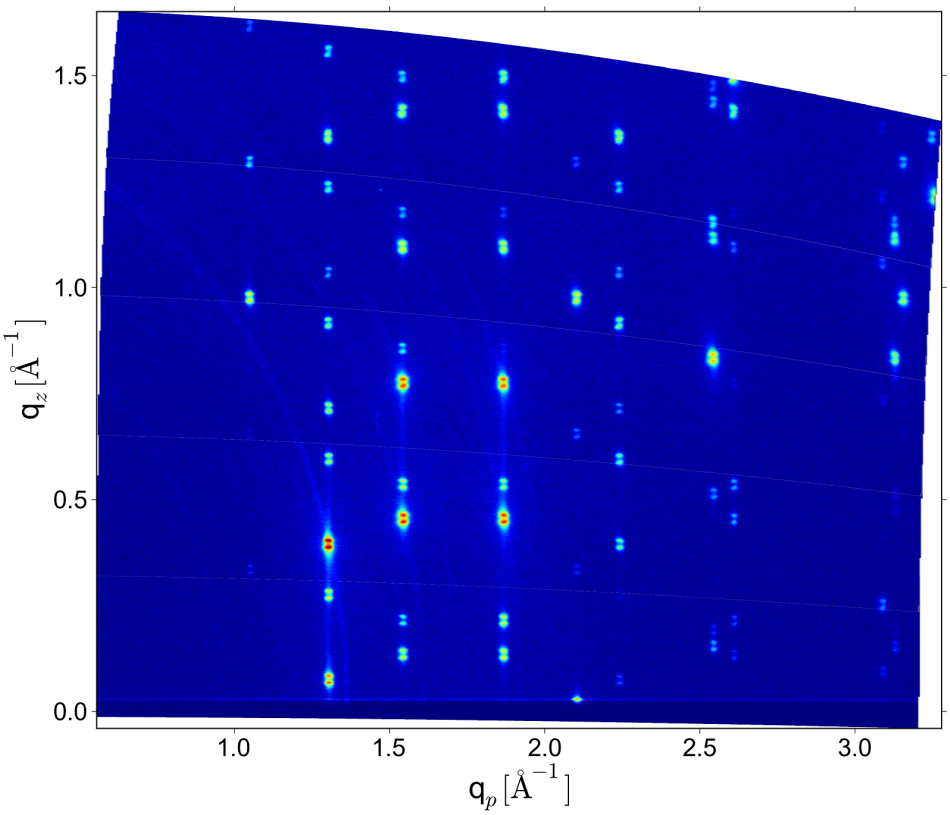

Figure 5.5: GIXD measurement for an incident angle of 0,15°

this effect a series of reciprocal space maps of two specific Bragg reflections at different incident angles α_i was recorded. Figure 5.6 depicts this series. The splitting occurs around the critical angle and vanishes for higher α_i. The origin of the peak splitting is that for α_i around the critical angle α_c one has to consider multiple scattering. The critical angles obtained from formula 3.6 (page 28) for NNN are $\alpha_{c,NNN}$=0,13° and for SiO_2 α_{c,SiO_2}=0,17°. So for α_i=0,15° the impinging X-ray beam is totally reflected at the film-substrate interface and the problem has to be treated with the distorted wave Born approximation (DWBA) since multiple scattering occurs. This doubling of scattering features is also observed in grazing incidence small angle scattering (GISAXS) for low-Z films, such as organic materials, on silicon substrates which is exactly the case here. Consequently the angle of incidence was changed to 0,11° in order to record exploitable diffraction patterns.

In chapter 3.1.3 dynamic scattering at surfaces is introduced. Four different scattering events result in two distinguishable exit angles. The calculated peak split in comparison with the actual measured Δq_z values from the experiment can be found in figure 5.7.

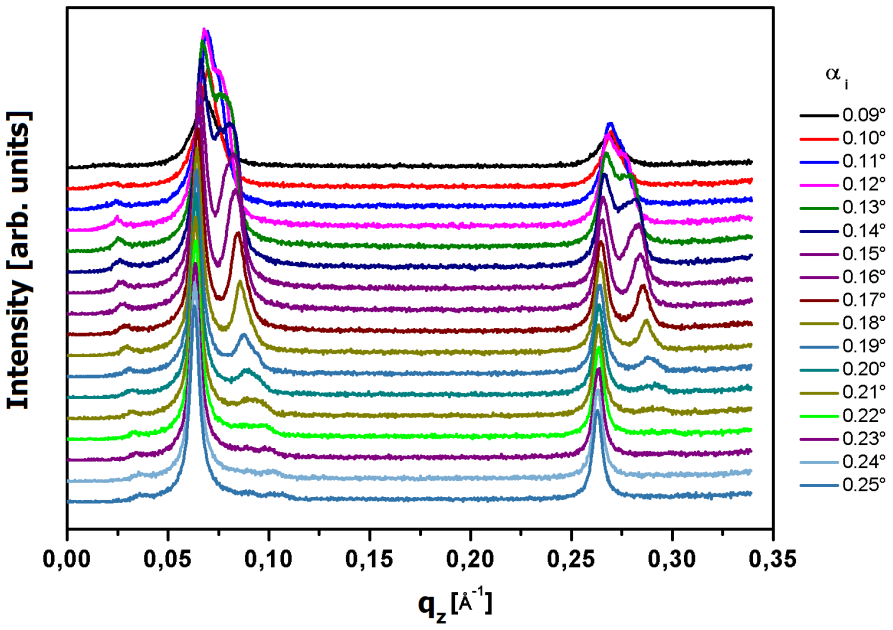

Figure 5.6: Series at different incident angles α_i from 0,9° to 0,25° each time in the range q_p = (1,2 - 1,4)Å^{-1} and q_z = (0 - 0,35)Å^{-1} corresponding to the Bragg reflexes 1-10 and -1-11 of the reciprocal space map in figure 5.8.

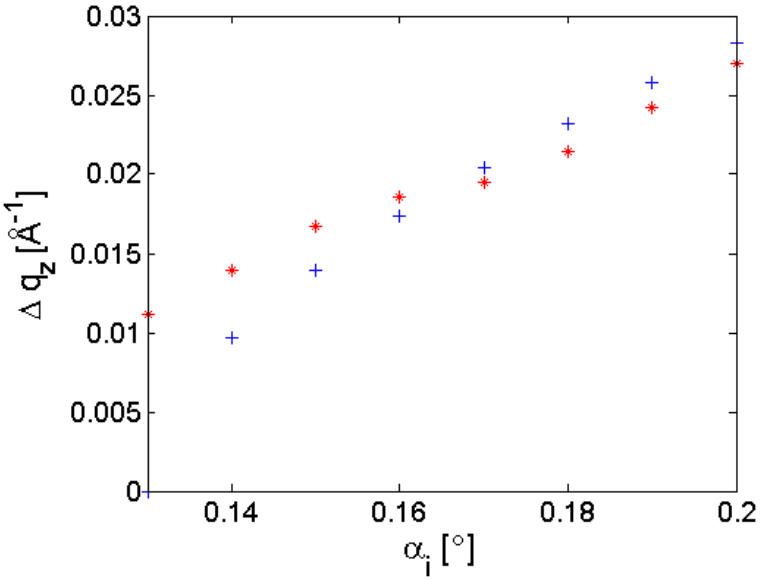

Figure 5.7: Comparison of the DWBA theory (blue +) and experiment (red *).

Theory and experiment show accordance for $\alpha_i > 0{,}15°$ where the DWBA is able to explain the observed peak doubling. Nevertheless DWBA fails for α_i close to α_c. One explanation for this might be the not perfectly oriented crystallites of the thin film. The doubling effect is even observed beyond α_c which is physically not possible when assuming perfectly oriented crystal layers since the X-ray beam should not penetrate into the material and be reflected at the thin film surface. Thus X-rays should not reach the substrate.

5.2 Indexation

Data transformation, i.e. transformation in reciprocal space, as well as indexation are done in PyGid. The software enables easy data treatment of GIXD measurements.

The right part of figure 5.4 shows the indexation of the home lab measurement and the respective values are in table 5.2. Figure 5.8 shows the respective measurement of the NNN thin film at HASYLAB at an incident angle of 0,11°. This measurement took around four hours and consists of five reciprocal space maps for different q_z intervals. The calculated indexation (white dots) in figure 5.8 comply with the actual measured peaks and therefore a matching unit cell is found.

The assumed contact plane is (0 0 1). The resulting unit cell in table 5.2 describes a monoclinic system. The obtained scattering pattern fulfils the criteria that the reflections are just visible for:

$$\begin{aligned} \text{h0l} &: \text{h} = 2\text{n}, \\ \text{0k0} &: \text{k} = 2\text{n}, \\ \text{h00} &: \text{l} = 2\text{n}. \end{aligned}$$

Therefore the symmetry is P 12_1/a 1, spacegroup 14.

Table 5.2: Lattice parameters for the NNN thin film sample for the indexation of the in-house data and the HASYLAB data.

	Home lab	HASYLAB
a [Å]	8,182	8,148
b [Å]	5,984	5,978
c [Å]	19,646	19,452
β [°]	85,75	94,58
ρ $[\frac{g}{cm^3}]$	1,315	1,314

Apparently already the home laboratory measurement led to good unit cell parameters. The first rough prove of the validity of the unit cell values is the mass density ρ. When assuming an occupation of the unit cell with two NNN molecules, the ρ-values of the table are within the range for carbon based aromatic molecular crystals.

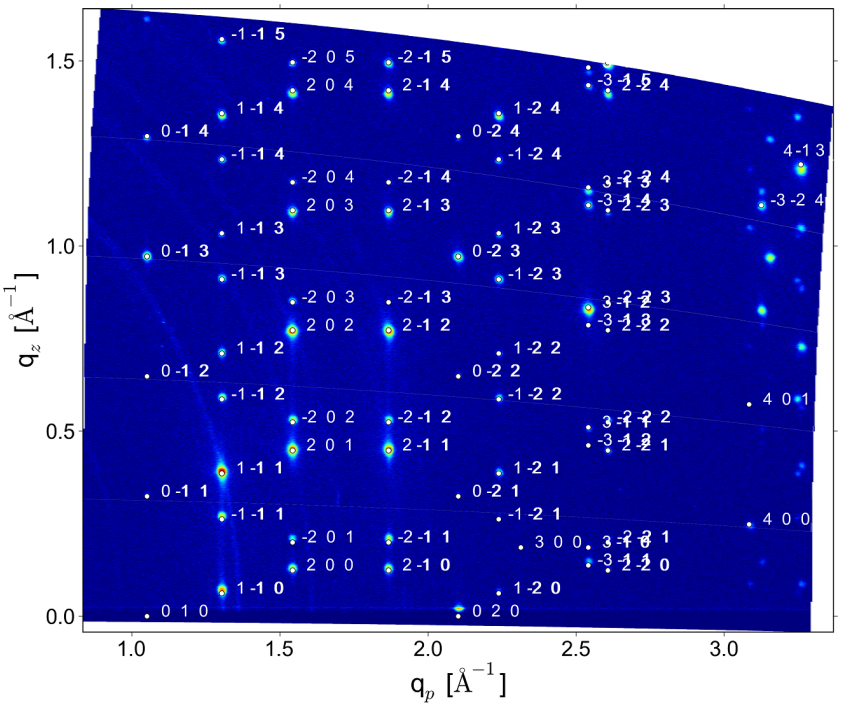

Figure 5.8: GIXD measurement of NNN with final indexation. Respective values for the unit cell can be found in table 5.2. Incident angle α_i was 0,11°.

5.3 Intensity Extraction and Intensity Correction

With the found unit cell values each reflection is assigned to a certain Bragg reflection and therefore a certain net plane distance in the crystal. In the next step the measured intensities of the various peaks were extracted. For the structure determination the indexed peaks in figure 5.9 were used. Each peak was fitted with a Gaussian curve and the background was subtracted. The area under the Gaussian corresponds to the intensity. To get the structure factors the measured intensity values have to be corrected (see chapter 3.3.1). Figure 5.10 shows the effect of the four correction factors. Dependent on the position of the peak the correction shows varying impact. For example the 1-11 Bragg reflection is heavily affected by Lorentz and area factor.

5.4 Molecular Conformation

The conformation of NNN was calculated by Egbert Zojer with the software Gaussian[46], which applies Self-Consistent Field (SCF) methods. The prior assumption was that the molecule is planar since conjugated oligomers usually adopt a planar or near-planar conformation[6]. The outcome of the calculation are all atomic positions of NNN in Cartesian coordinates. The result of this calculation can be found in the figure 5.11. The planar molecule is represented by bonding lengths between all atoms in a table.

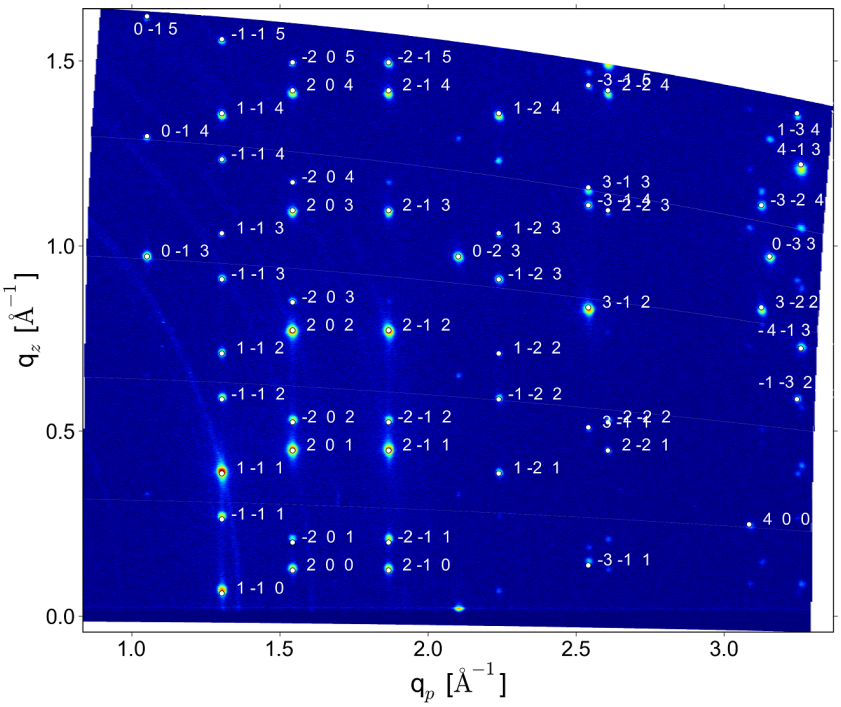

Figure 5.9: Extracted intensities of the HASYLAB GIXD measurement of NNN. All in all 60 peaks were extracted.

5.5 Structure Simulation

To summarize the information there is so far:

- Unit cell parameters
- Spacegroup symmetry
- Number of molecules in the unit cell
- Molecular conformation from calculation
- The structure factors from the experiment

The software FOX needs all this information as input. In a first attempt the position of the basis is fixed to 0 0 0 therefore the molecular positions are 0 0 0 for the first molecule and 0,5 0,5 0 for the second molecule in fractional coordinates of the unit cell. Furthermore the molecules are assumed to be rigid. The software would have capabilities to optimize intra-molecular distances as well but due to much too poor data from GIXD experiments this is not advisable. Because of that FOX does not take all peaks into account. The considered 38 peaks are: 1-10, -1-11, 1-11, -1-12, 0-13, 1-12, 200, -201, -1-13, 201, -202, 1-13, 0-14, 202, -203, -1-14, 2-10, -2-11, 1-14, 203, 2-11, 0-15, -204, -2-12, 2-12, -1-15, 204, -205, 2-13, 0-22, 1-21, -1-22, 0-23, 2-14, 1-22, -2-15, -1-23, 1-23. The reason is that peaks with high q-values correspond to intra-molecular distances which are fixed due to the rigid body assumption.

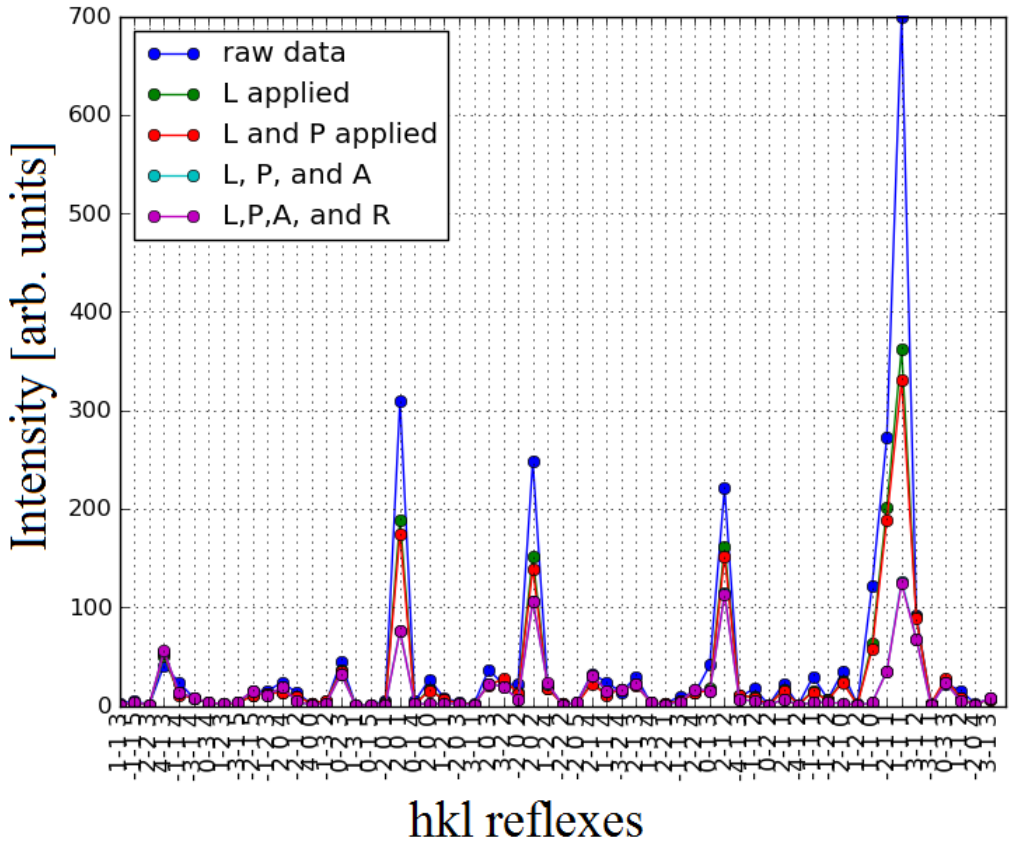

Figure 5.10: Correction of the extracted intensities. Starting from the raw data the evolution of the intensities is displayed where L stands for the Lorentz factor, P for the polarization factor, A for the area factor and R for the rod interception factor. The turquoise line is identical with the magenta line due to the minor impact of R.

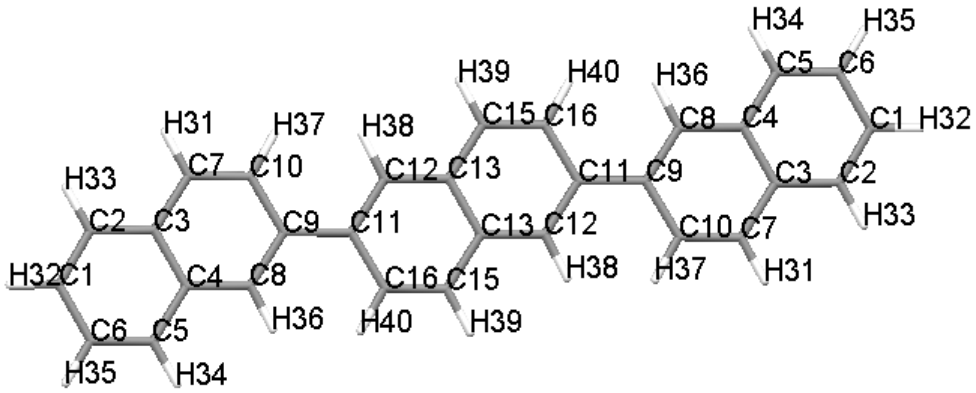

Atom 1	Atom 2	Length [Å]	Atom 1	Atom 2	Length [Å]
C1	C2	1,372000	C15	H39	1,083000
C1	C6	1,411164	C16	H40	1,078996
C1	H32	1,082004	C17	C18	1,383011
C2	C30	1,413996	C17	H41	1,080001
C2	H33	1,083007	C18	C19	1,425001
C3	C4	1,424002	C18	C21	1,487000
C3	C7	1,415000	C19	C20	1,367000
C4	C5	1,416999	C19	H42	1,078997
C4	C8	1,370000	C20	H43	1,082996
C5	C6	1,083005	C21	C22	1,382005
C5	H34	1,081998	C21	C26	1,425046
C6	H35	1,081998	C22	C23	1,412997
C7	C10	1,366467	C22	H44	1,079996
C7	H31	1,080002	C23	C24	1,425002
C8	C9	1,425001	C23	C30	1,417014
C8	H36	1,487000	C24	C25	1,413997
C9	C10	1,079005	C24	C27	1,413997
C9	C11	1,382987	C25	C26	1,365996
C10	H37	1,079005	C25	H45	1,083003
C11	C12	1,382987	C26	H46	1,078992
C11	C16	1,425245	C27	C28	1,372003
C12	C13	1,411001	C27	H47	1,082994
C12	H38	1,080008	C28	C29	1,411003
C13	C14	1,420999	C28	H48	1,081997
C13	C20	1,415630	C29	C30	1,371005
C14	C15	1,415994	C29	H49	1,082003
C14	C17	1,409997	C30	H50	1,083004
C15	C16	1,365999			

Figure 5.11: Bonding lengths of the NNN molecule. The depicted NNN molecule with labelled atoms allows the allocation of the bonds.

Starting from an initial guess for the orientation of the molecules in the unit cell the software probes various orientations in real space and optimizes the χ^2 between calculated and observed structure factors. Figure 5.12 displays the calculated and the measured structure factors.

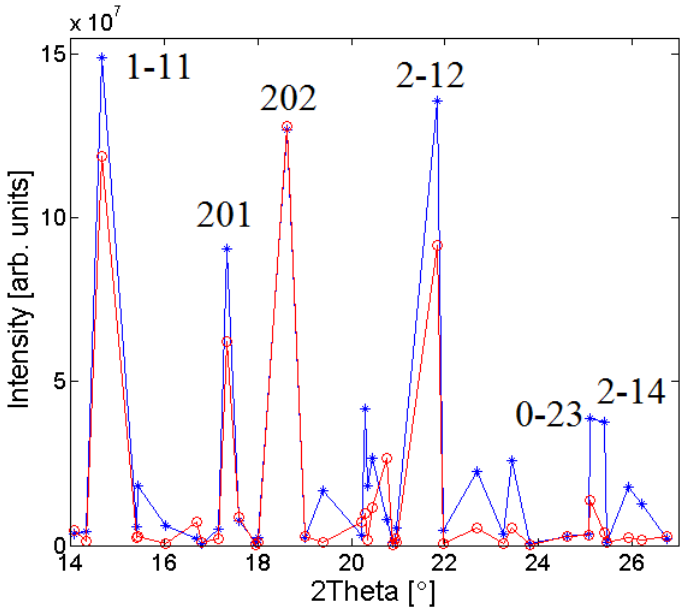

Figure 5.12: Observed (blue line) vs. calculated (red line) structure factors. Just data up to approximately 2θ=27° is considered in the refinement since higher angles refer to intramolecular distances.

5.6 Structure Solution

The final solution for the structure of NNN on SiO_2, displayed in figure 5.13, is highly reproducible. The molecules arrange in every simulation run in a herringbone motif. Even when reducing the amount of information, e.g. omitting the symmetry by assuming a triclinic arrangement in FOX, the simulation yields qualitatively equal results.
In order to check the obtained structure solution of NNN, a diffraction pattern from this found solution was calculated and is compared in figure 5.14 with the measured reciprocal space map. Simulated and measured Bragg reflections show satisfying coverage and the intensities do fit as well. The quality indicators for the crystal structure solution are the R factor which is 0,43 and the weighted R factor which is 0,65 for the NNN structure. Those values were automatically calculated by FOX and manually checked in MatLab.

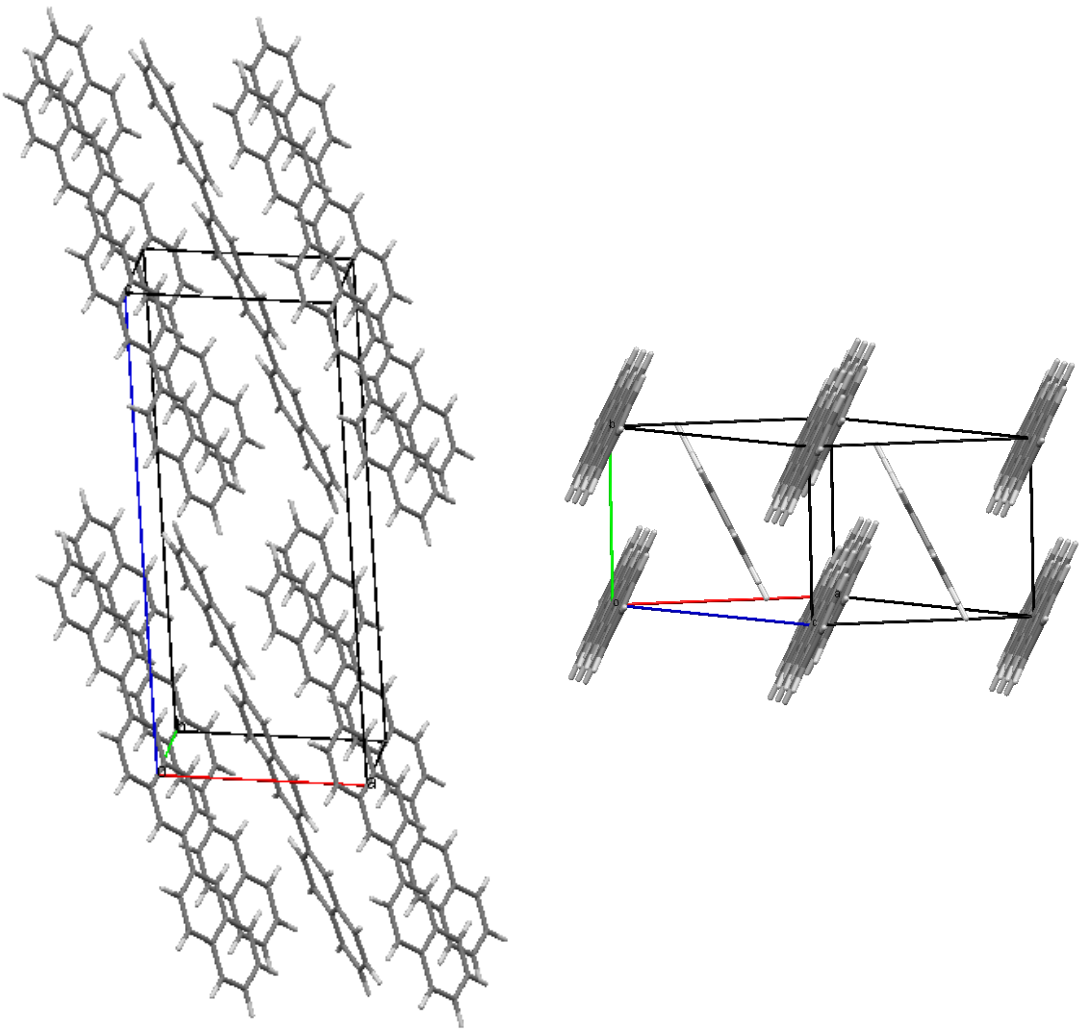

Figure 5.13: Determined molecular packing of the NNN molecules. The blue axis is the out-of-plane axis for the thin film sample, i.e. the molecules stand almost upright on the surface.

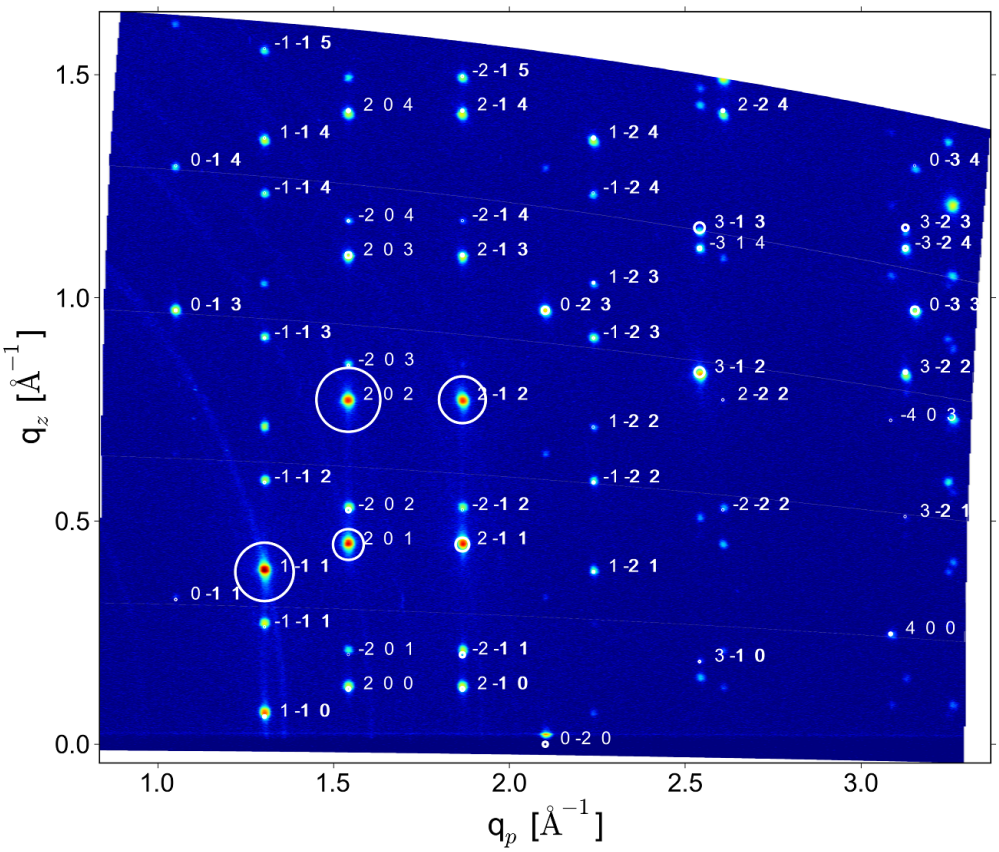

Figure 5.14: Comparison of the calculated diffraction pattern of the FOX simulation (white circles) and the GIXD measured reciprocal space map. The area within the circles indicates the intensity of the respective Bragg peaks for the found solution.

5.7 NNN on HOPG

A NNN thin film was as well prepared on HOPG. Due to the AFM picture in figure 5.15 it is assumed that most of the molecular backbones are parallel to the surface and the molecules therefore lie on the surface. The AFM measurement shows different morphologies, needle-like structures and terraces, which indicates that there are standing molecules present as well. The result of the $\Theta/2\Theta$ measurement in figure 5.16 confirms the expectation after the AFM image by revealing multiple orientations which are present on the graphite substrate.

After precharacterisation in the home laboratory an extensive GIXD measurement was performed at HASYLAB. The measurement was taken for 2Θ = 2° - 30°, with step size of $\Delta 2\Theta$ = 0,05° and a integration time of 2s. The NNN bulk phase unit cell parameters explain with four different orientations and therefore four different contact planes, namely (1,-1,1) overlapping with (1,1,1) due to the monoclinic symmetry, (2,-1,2) overlapping with (2,1,2), (2,0,2) and (0,0,1), almost all peaks of the obtained reciprocal space map in figure 5.17. The orientations correspond to strong reflexes of the reciprocal space of NNN on SiO_2 which indicate preferred orientations.

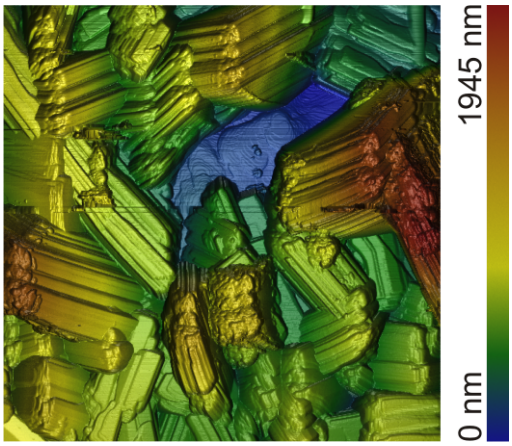

Figure 5.15: The sample grown on the HOPG surface shows terrace structure (blue region in the figure) and needle-like structure, which is typical for on the surface lying molecules. The parallel lines in the middle of the image might be artefacts which occur due to the height of the sample.

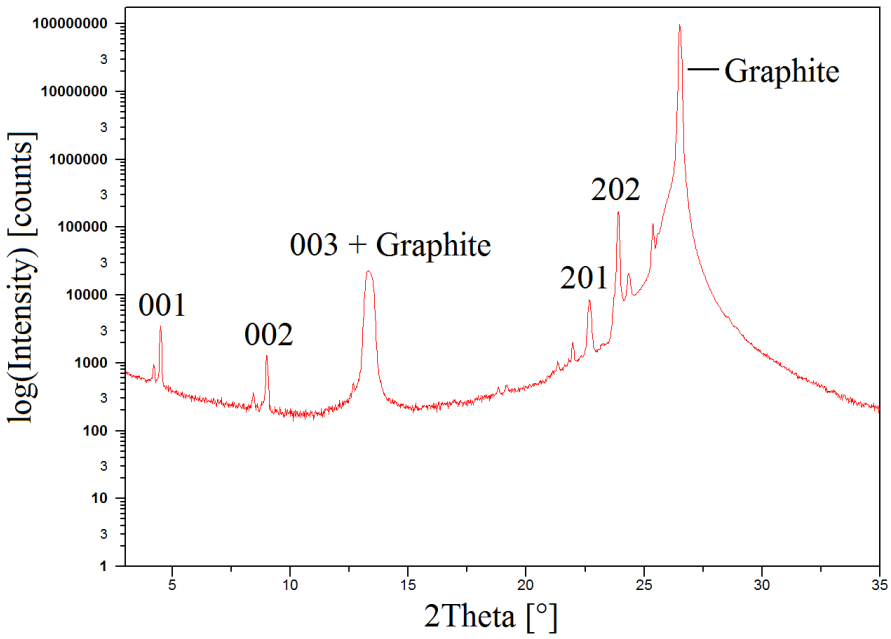

Figure 5.16: Specular scan of NNN on HOPG with logarithmic scale. Reflexes from standing unit cells (001, 002, 003) and lying unit cells (201, 202) are indicated and graphite Bragg reflections (001, 002) were identified.

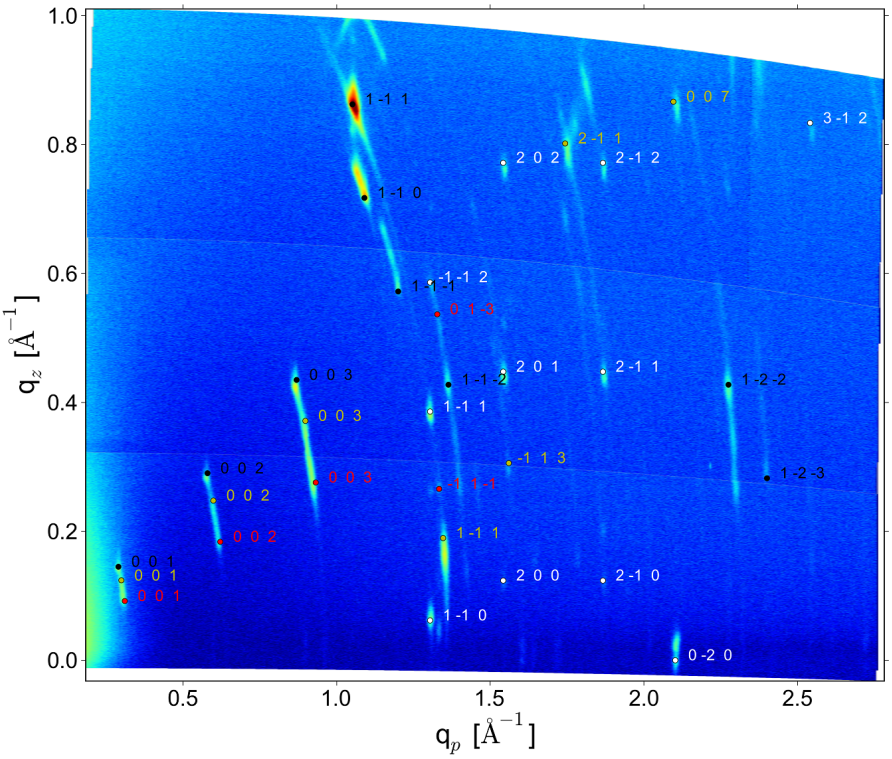

Figure 5.17: Indexation of the GIXD measurement of NNN on HOPG. The incident angle α_i was 0,2°. Different colors refer to different molecular orientations, whereas red is the (1,-1,1) contact plane, yellow is (2,-1,2), black is (2,0,2) and white corresponds to upright standing molecules with (0,0,1) contact plane.

5.8 Rietveld Refinement of NNN Powder

As a last step NNN powder was analysed using standard 3-D powder X-ray diffraction (XRD). The powder was ground for 1 h 25 min in a mortar and mounted with a specimen holder in the PANalytical XRD (see figure 5.18). The powder was spread with a razor blade. However, this might introduce a certain texture to the sample. The specular measurement was acquired from $2\Theta = 3°$ to $2\Theta = 40°$. The step size was 0,02° with 6s data acquisition time per step.

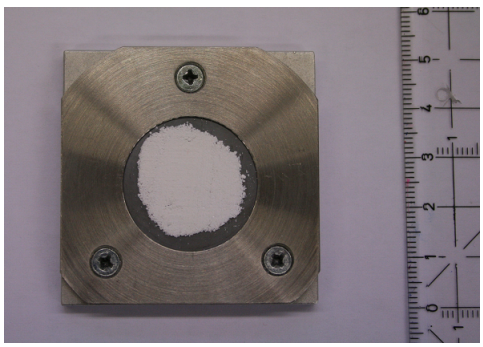

Figure 5.18: NNN powder in specimen holder.

The further data processing was performed in the software HighScore where a Rietveld refinement was done. As explained in section 2.2.4 the Rietveld refinement procedure optimizes a structure to a measured scattering profile. The reference structure is the found NNN structure from the thin film sample. First possible systematic uncertainties, arising from misalignments of the sample, are corrected. Texture effects can also be corrected to some extend. Other parameters, lattice constants or peaks shapes, are then refined yielding in the unit cell parameters presented in table 5.3.

Table 5.3: Comparison of the obtained unit cell values for the Rietveld refinement with the indexed unit cell of the GIXD measurement.

	GIXD	Rietveld	Differences
a [Å]	8,148	8,137	0,011
b [Å]	5,978	5,966	0,012
c [Å]	19,452	19,625	0,173
β [°]	94,58	94,27	0,31

The obtained quality factors are R = 0,29 and wR = 0,36 which are better than the obtained values from the simulation. However when comparing the unit cell in the measured reciprocal space map the misfit of the Rietveld indexation is bigger than the misfit of the original indexation. This shows the general uncertainty for GIXD data and the applied data treatment. The reason for this is the poor data quality and quantity of GIXD measurements compared to powder diffraction experiments. Moreover a bigger offset for the c-value can be seen in table 5.3 which might be the consequence of some systematic error. Possible texture introduced in the powder sample preparation affects the recorded powder pattern and can lead to higher or lower pronounced peaks as in figure 5.18.

5.9 Conclusion

NNN thin film samples on SiO_2 and HOPG surfaces were examined. The observed Bragg peak doubling for the thin film sample of NNN on SiO_2 could be accounted to the dynamic scattering effects and circumvented by measuring under a different incident angle.

The measured HASYLAB-GIXD-pattern for NNN on SiO_2 has alone-standing and strong reflections which alleviated the indexation and the assignment of the crystal symmetry. However it is noticeable that d_{hkl}=19,59Å obtained from the specular measurement and the calculated value of the unit cell d_{hkl}=19,39Å do not match satisfyingly. The reason for this might be a systematic error for the out-of-plane values (q_z values) which was not found during this work. Nevertheless the structure resolution was successful and a solution was found. The molecules arrange in a herringbone pattern. This result of the FOX simulation was reproducible and the density ρ as well as the results from the specular scan do complete the picture. Additionally the result

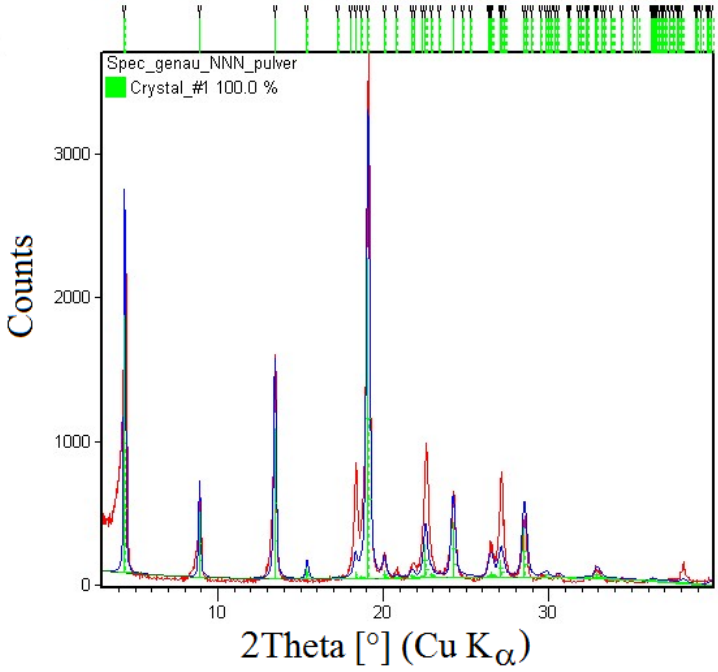

Figure 5.19: Rietveld refinement of a NNN powder sample. The red line is the measured powder diffraction pattern, the blue line the calculated intensity distribution from the Rietveld refinement and the green lines indicate the considered peaks.

confirms the found prediction after the method of Desiraju and Gavezzotti (see chapter 1.2) which is as well a herringbone packing.

The specular scan of the NNN film on HOPG showed Bragg peaks of multiple molecular orientations. Therefore a structure resolution from the GIXD measurement was not feasible. However it was possible to index the reflections with the obtained unit cell from the NNN-on-SiO_2-sample. Four orientations explain the features of the reciprocal space map. Thus the same NNN phase is present on HOPG and on SiO_2.

Due to the thickness of almost 1μm those NNN films do not exhibit a thin film phase but rather the bulk phase. This led to the possibility of a Rietveld analysis of a measured NNN powder diffraction pattern. The obtained structure solution fits qualitatively although the quality factors (R and wR factor) can in general not compete with the values of standard 3-D powder XRD experiments. The reason is that the quality and amount of data of GIXD and XRD measurements can not be compared which might explain the rather disappointing values for R and wR.

6 Dibromo-Indigo (TP)

Dibromo-Indigio, colloquially known as Tyrian Purple (TP), was already used as dye in ancient times. The chemical formula is $C_{30}H_8Br_2N_2O_2$ and the structural formula is displayed in figure 6.1.

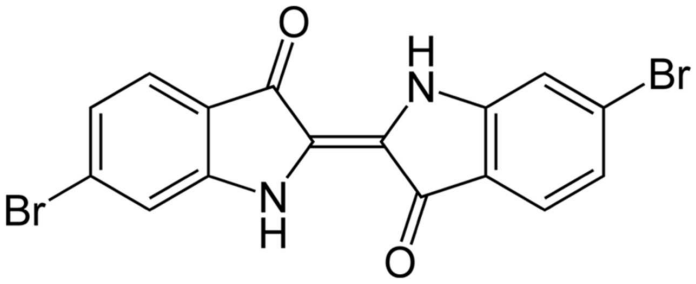

Figure 6.1: Schematic structure of TP

TP is a conjugated molecule with strong hydrogen bonds that reinforce π-stacking[41] and therefore exhibit interesting electronic properties. Thin films of TP got in the focus for applications in organic semiconductors were surface induced effects play an important role. Various TP thin film sample were analysed. Three samples were manufactured with hot wall epitaxy on SiO_2 at different substrate temperatures by Rizwan Ahmend from JKU Linz. The analysis of those samples can be found in section 6.1. Additionally various TP thin film samples e.g. on polyethylene (PE) or on copper iodide (CuI) surfaces were manufactured by Mihai Irimia-Vladu and Eric Glowacki also from JKU Linz. Those samples show interesting surface-induced behaviour and will be discussed in section 6.2.

6.1 Tyrian Purple Bulk Phase

The TP thin films on SiO_2 were grown at three different substrate temperatures, namely 50°C, 100°C and 150°C, and have a film thickness of approximately 250nm. From the specular scan it is apparent that the thin films of the samples by Rizwan Ahmed crystallized in the already known bulk phase of TP. Nevertheless a structure resolution was carried out in order to learn more about the quality of crystal structure solutions from GIXD measurements. All three sample were analysed using AFM and are depicted in figure 6.2.

In a first step in-house GIXD measurements were done which are depicted in figure 6.4. All picture series (figure 6.2, 6.3 and 6.4) show the influence of the substrate

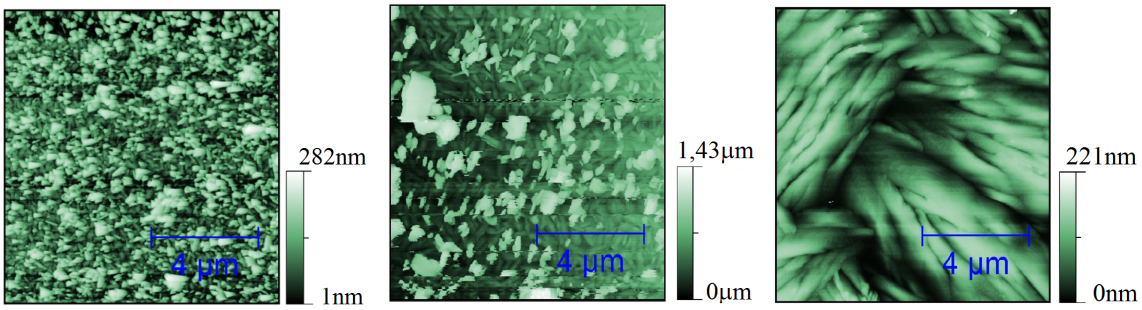

Figure 6.2: AFM measurements of the TP samples grown at substrate temperature 50°C, 100°C and 150°C from left to right.

temperature on the crystallinity of the thin film. The higher the temperature the bigger the crystalline structures (in the right picture in figure 6.2) and the sharper the peaks (in the right picture in figure 6.4). The specular scans in figure 6.3 do also confirm this by showing much higher intensities the higher the applied substrate temperature in the HWE procedure. With that knowledge only the sample grown at 150°C was used for further investigation.

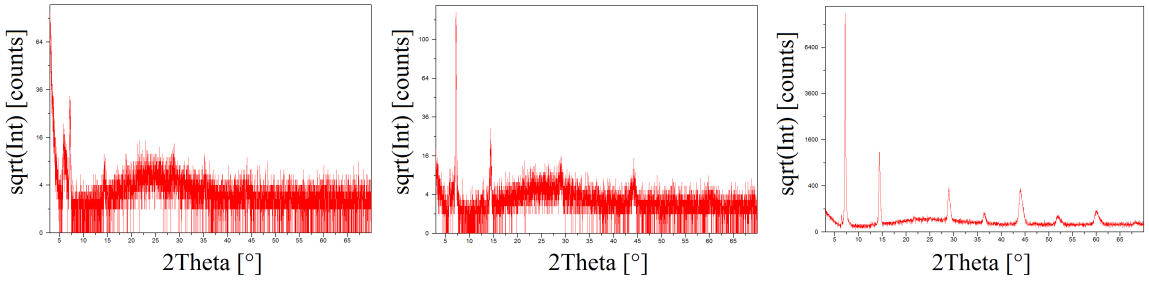

Figure 6.3: Specular measurements of the TP samples at substrate temperature 50°C, 100°C and 150°C.

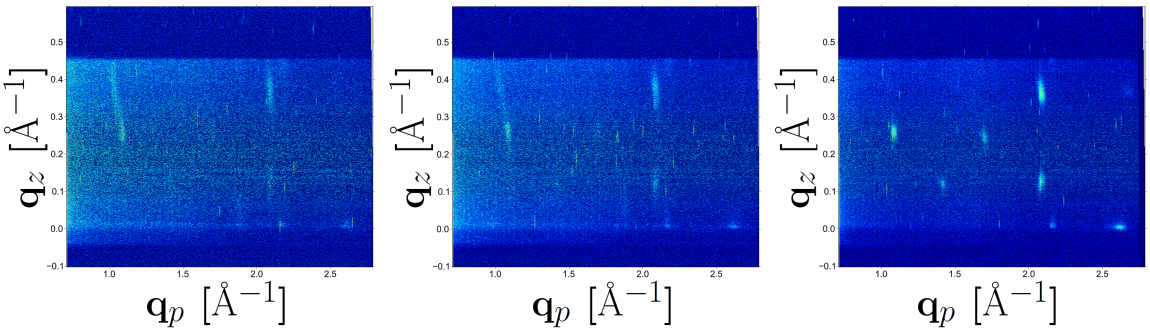

Figure 6.4: GIXD measurements of the TP samples at substrate temperature 50°C, 100°C and 150°C. A steady increase of the crystallinity is observed when increasing the substrate temperature for the HWE.

6.1.1 Indexation

The measurement of the 150°C-sample (figure 6.5) was performed at the W1 beamline in Hamburg by Ingo Salzmann in September 2012.

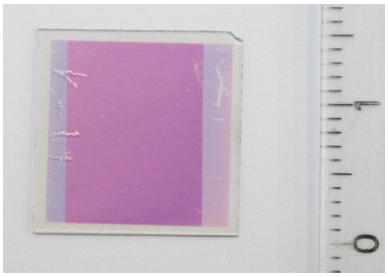

Figure 6.5: The TP thin film sample on SiO_2, grown at 150°C.

The reciprocal space map in figure 6.6 shows clear peaks and good accordance with the found monoclinic indexation. The respective mass density is 1,2 $\frac{g}{cm^3}$ with two TP molecules in the unit cell. The found indexation in the first column in table 6.1 is in good accordance with already published structure solutions with P 1 2_1/c 1 symmetry. The contact plane of the unit cell on the substrate surface is the (1 0 0) plane. As can be seen in the table, the volume does not deviate much and therefore the densities ρ are approximately equal.

Table 6.1: Unit cell parameters for TP in comparison to literature values.

	This work	[42]	[43]
a [Å]	12,47	12,60	12,609
b [Å]	4,80	4,85	4,842
c [Å]	11,65	11,50	11,611
β [°]	103,24	104	104,42
V [Å^3]	679	682	687

6.1.2 Molecular Conformation

The conformation was calculated with Gaussian by Egbert Zojer. The molecule was assumed to be of planar shape which is a reasonable approximation due to the strong double bond between the bromine-indoxyl groups and hydrogen bonds between O and H. In table 6.2 the bonding lengths of the Molecular conformation of Zojer and the experimentally obtained structure from [43] are compared.

Higher deviations Δl can be observed for bonds with hydrogen and especially the N-H bonds show a mismatch of 0,3Å. The reason for this is that X-ray scattering is not very sensitive to hydrogen due to its interaction with electrons.

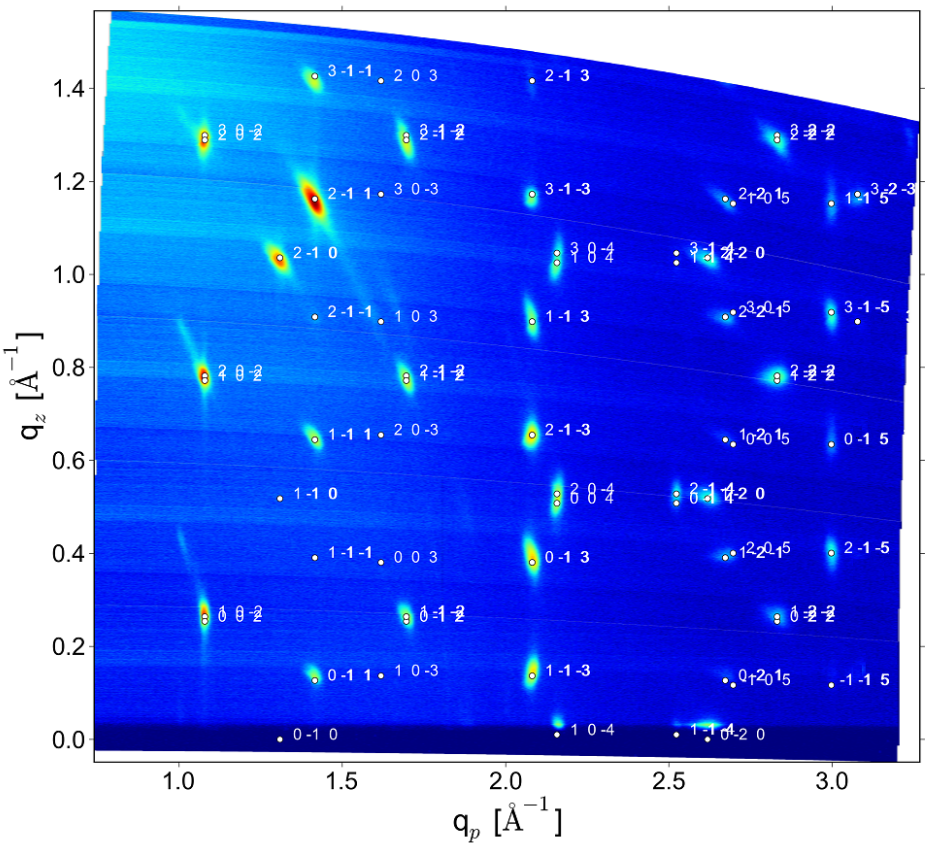

Figure 6.6: Indexation of the reciprocal space map of the TP thin film on SiO_2 surface. The incident angle for the measurement was 0,15°.

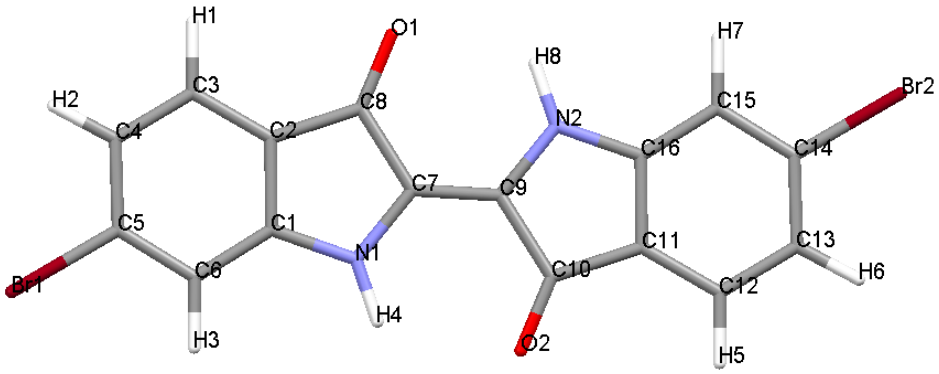

Figure 6.7: Numered atoms of TP to compare bonding lengths in table 6.2.

Table 6.2: Comparison of the calculated bonding lengths $l_{bond,cal}$ from the software Gaussian, the experimentally obtained values $l_{bond,exp}$ from [43] and the differences Δl. In order to allocate the numbered atoms see figure 6.7

Atom1	Atom2	$l_{bond,cal}$ [Å]	$l_{bond,exp}$ [Å]	$\lvert\Delta l\rvert$ [Å]
N1	H4	1,011704	0,695823	0,315881
N2	H8	1,011703	0,696002	0,315701
C4	H2	1,082931	0,883573	0,199358
C13	H6	1,082930	0,884008	0,198922
C3	H1	1,085506	0,987756	0,097750
C12	H5	1,085515	0,988005	0,097510
C6	H3	1,083431	0,986866	0,096565
C15	H7	1,083430	0,987001	0,096429
C3	C4	1,392104	1,367449	0,024655
C12	C13	1,392100	1,368347	0,023753
C2	C8	1,468019	1,446659	0,021360
C10	C11	1,468014	1,446662	0,021352
C5	C6	1,394535	1,375033	0,019502
C14	C15	1,394536	1,377005	0,017531
C5	Br1	1,908256	1,894665	0,013591
C14	Br2	1,908260	1,897003	0,011257
C9	N2	1,380961	1,369996	0,010965
N1	C7	1,380955	1,370002	0,010953
C10	O2	1,232645	1,238001	0,005356
C8	O1	1,232645	1,237982	0,005337
C11	C12	1,394282	1,399005	0,004723
C7	C9	1,359848	1,363999	0,004151
C6	C1	1,394525	1,390651	0,003874
C16	C11	1,415862	1,411995	0,003867
C1	C2	1,415862	1,412318	0,003544
C15	C16	1,394525	1,390998	0,003527
C2	C3	1,394286	1,397385	0,003099
C1	N1	1,386181	1,383333	0,002848
C7	C8	1,491679	1,489004	0,002675
C9	C10	1,491675	1,489002	0,002673
N2	C16	1,386183	1,384003	0,002180
C4	C5	1,403652	1,402944	0,000708
C13	C14	1,403651	1,402994	0,000657

6.1.3 Structure Solution

34 peaks were extracted for the FOX simulation whereas the double peaks, namely -202 and 201, -2-12 and 2,-1,1, 200 and -201, -402 and 400, were fitted in Fityk[47]. The simulation led to a reproducible result: TP packs in a parallel stacked arrangement with tilted adjacent stacks (figure 6.8). The distance between the π-stacking planes is 3,45Å. This result is equivalent within an expected uncertainty to the already known

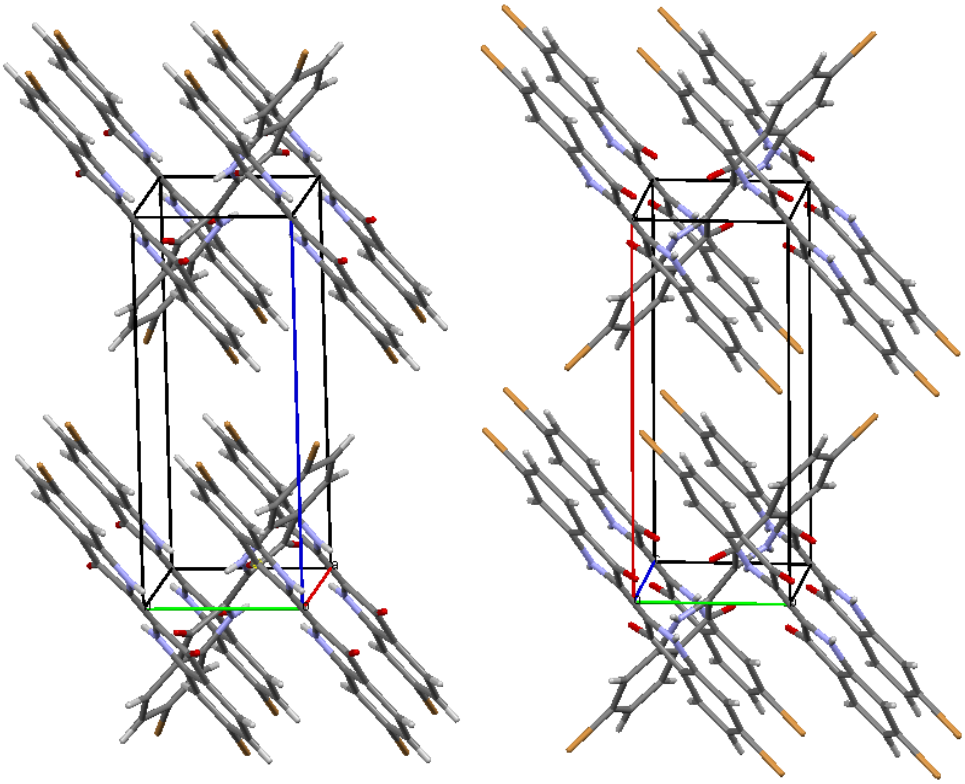

Figure 6.8: Molecular arrangement of TP in the unit cell. On the left the result of this work and on the right the structure result from [43].

structure solutions. The only thing to mention is the position of bromine which does not match. In the GIXD solution the molecule positions are the same but the TP molecules are rotated around the molecular backbone by 180°. Even artificially rotating the molecules initially before starting the simulation yielded in the same result and therefore a mismatch between the already published and the found GIXD structure solution. Apart from that the results are in good accordance and the measured and the calculated intensities match qualitatively in figure 6.9.

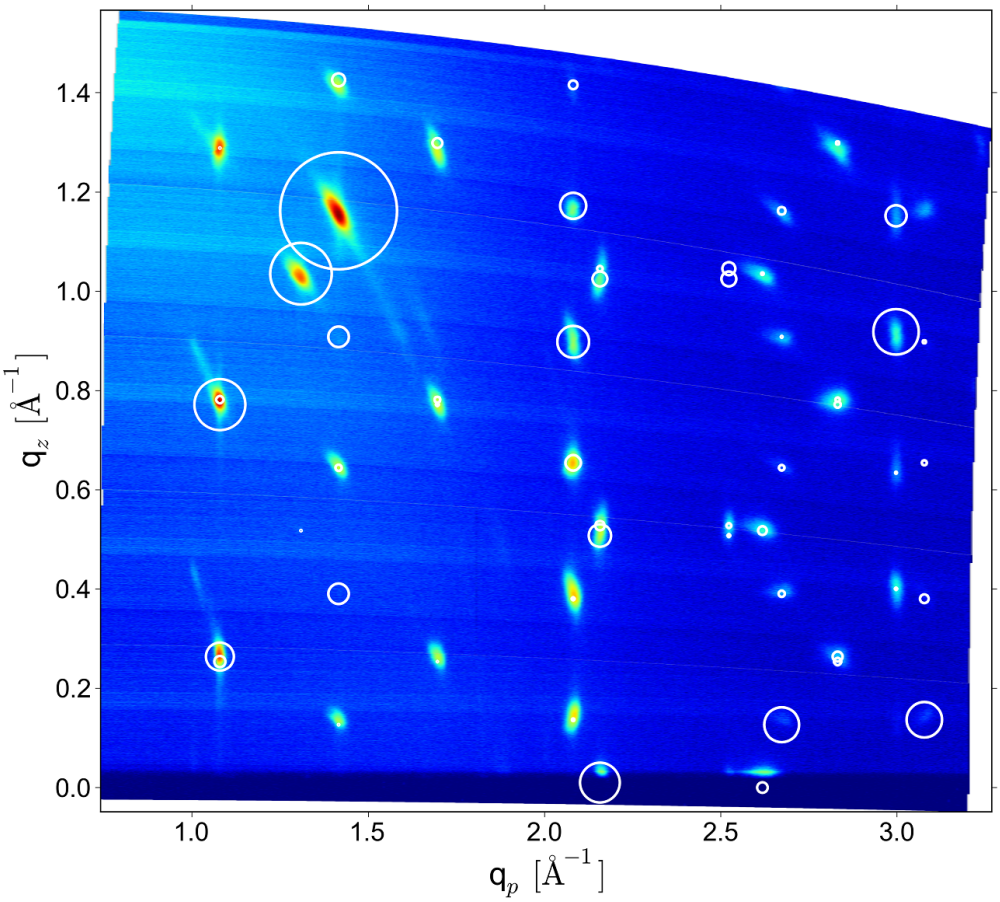

Figure 6.9: Calculated intensities from the obtained TP bulk structure solution as white circles in the measured reciprocal space map.

6.2 Tyrian Purple Thin Film Phase

TP thin films on various substrates (glass, n-octyl silane (OTS), CuI, tetratetracontane (TTC), PVA, PE, shellac) were analysed. The films have a thickness of 50nm, 80nm and 250nm. The GIXD-measurements in the home laboratory showed the poor quality of the spin coated samples. Nevertheless two samples (TP on PE and TP on CuI) showed in comparison better defined features in the scattering images. Additionally those samples are of interest since the molecules are supposed to lie on CuI and stand upright on PE. Depending on the molecular alignment the transition dipoles of the overlapping π-orbitals (π-stacking) point in different directions, parallel to the surface for standing molecules and perpendicular for face-on aligned (lying) molecules. This results in oriented charge mobility either parallel or perpendicular to the surface and explains the observed charge transport properties.

6.2.1 Tyrian Purple on Polyethylene

Due to the standing molecules and the resulting charge mobility, organic field effect transistors (OFETs) can be build with TP thin films on a PE surface. The specular scan is depicted in figure 6.10. The sample was GIXD-measured at HASYLAB and indexed (figure 6.11). The found unit cell has triclinic symmetry. The unit cell parameters are: a = 3,83Å, b = 5,84Å, c = 15,85Å, $\alpha = 104{,}5°$, $\beta = 92{,}4°$ and $\gamma = 93{,}2°$. The resulting mass density in this case with one TP molecule in the unit cell computes to $1{,}2\frac{g}{cm^3}$ which corresponds to the mass density of the bulk structure.

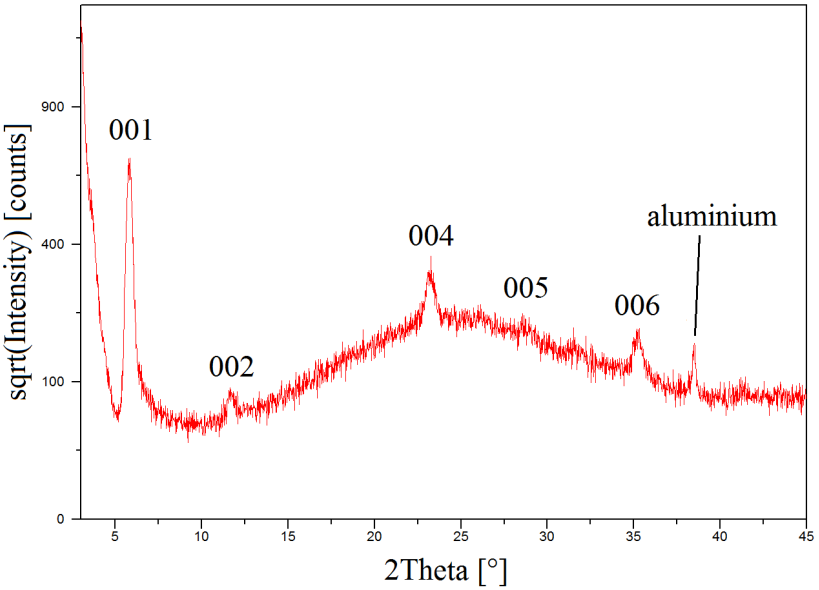

Figure 6.10: Specular scan of a TP thin film on PE surface. The positions and intensity distribution of the {0 0 l} series correspond to the measured pattern at $q_z = 0\text{Å}^{-1}$ in figure 6.13. The reason for the measured aluminium peak is an aluminium electrode on the sample.

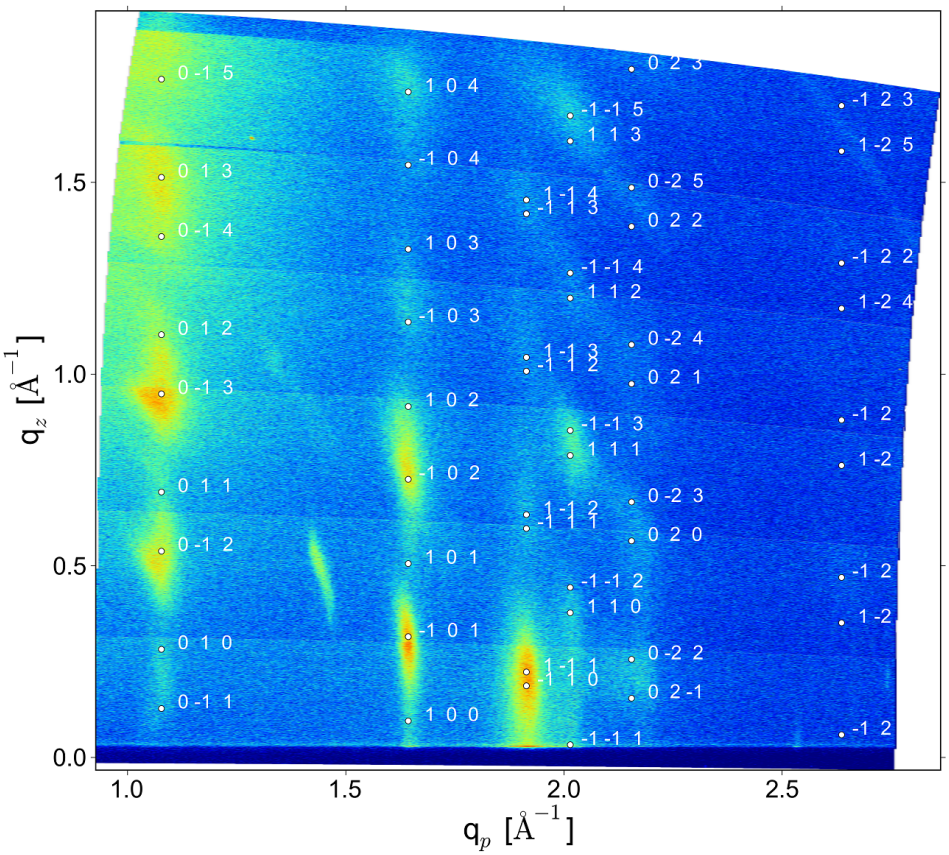

Figure 6.11: HASYLAB measurement with best found indexation of the TP thin film on PE. The peaks are blurred but five rods are clearly distinguishable. The contact plane is (0 0 1).

6.2.2 Tyrian Purple on Copperiodide

The application of TP films on CuI with face-on aligned molecules are diodes (OLEDs). A specular scan is depicted in figure 6.12. The GIXD measurement in figure 6.13 shows mosaicity. The found indexation for TP on PE does not fit perfectly but the peaks at $q_z = 0\text{Å}^{-1}$ have the exact same pattern as the specular scan of the TP film on PE in figure 6.10. The reciprocal space map of a lying unit cell, i.e. lying molecules in this

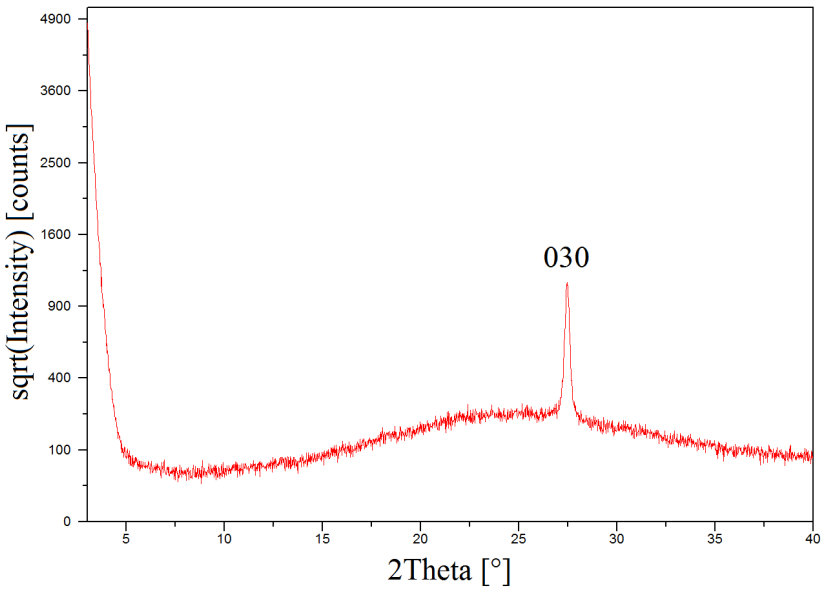

Figure 6.12: Specular scan of a TP thin film on CuI surface. Merely the 030 Bragg reflection is visible.

case, contains at $q_z = 0\text{Å}^{-1}$ the same information as a specular scan of a standing unit cell. On the PE surface TP molecules are standing. This proves that the same thin film phase is present on both surfaces.

Hence that the obtained information for lying and standing TP molecules was merged and in order to get a more precise impression of the molecular orientation on the surfaces a FOX-simulation was accomplished. The simulation of the molecular arrangement was done for the TP-on-PE-sample since the Bragg reflexes are better defined. It was possible to extract eight peaks which lead to the result in figure 6.14. Due to the poor data quality the results are not satisfyingly accurate nor exactly reproducible. However an educated idea about a possible alignment of the TP molecules on PE and therefore about the alignment of TP on CuI was obtained.

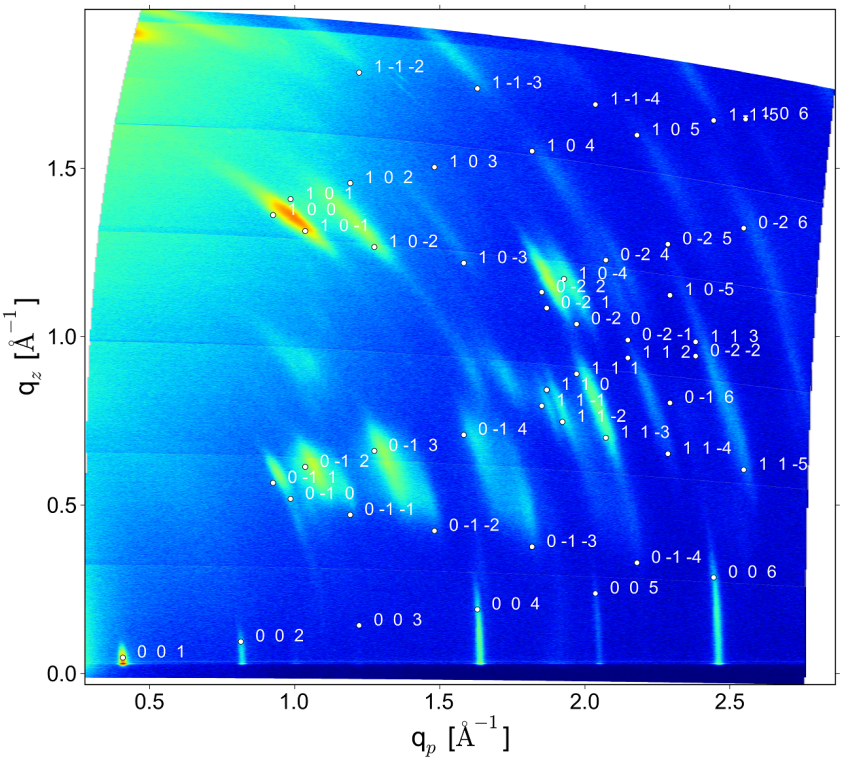

Figure 6.13: HASYLAB measurement with best found indexation of the TP thin film on CuI. The contact plane is (1 -1 1). The intensity distribution at $q_z = 0$Å^{-1} corresponds to the specular scan of the TP film on PE in figure 6.10.

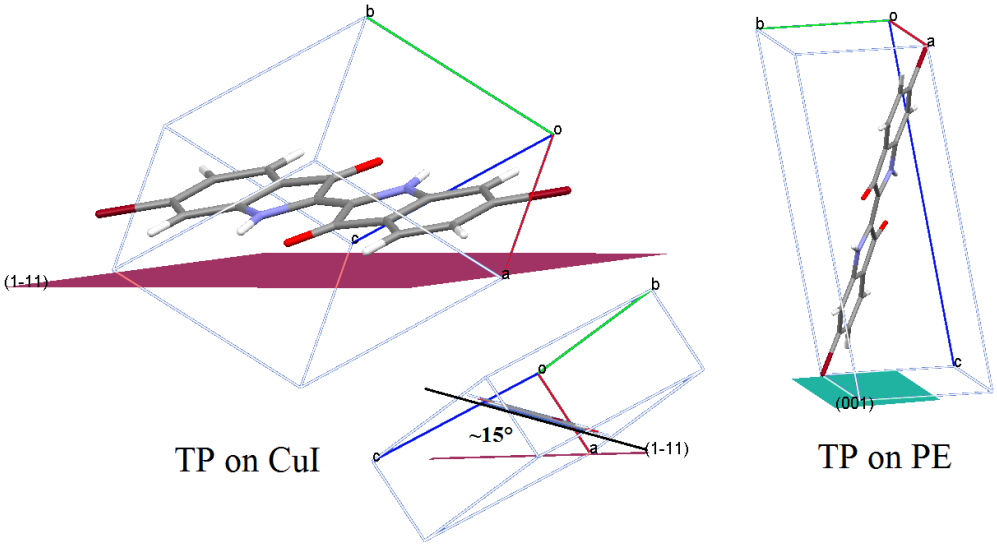

Figure 6.14: Resulting molecular position on a CuI surface on the left side. The contact plane is (1 -1 1) which is one of the strongest peaks in the GIXD measurement 6.11. The lying molecule is tilted by approximately 15°. On the right side an upright standing molecule on a PE surface with contact plane (0 0 1) is displayed.

6.3 Conclusion

The samples by Rizwan Ahmed of TP on SiO_2 surface crystallized in the already known bulk phase. Nevertheless a structure resolution was done in order to analyse the capabilities of the GIXD approach for structure determination. The obtained results for the lattice parameters are in good accordance to literature values however as in chapter 5.9 the obtained out-of-plane values, i.e. lattice parameter a, have the biggest off-set. The resulting structure is a parallel stacked arrangement which was found with just 34 extracted intensities whereas single crystal diffraction usually uses thousands of Bragg peaks. The qualitative comparison of the obtained and the already published structure showed accordance however the position of the bromine atom does not fit. Several runs even with artificially changed bromine position yielded in the same result.

The very interesting and application-near samples of Glowacki et al. were more difficult to interpret. All films showed low crystallinity and had therefore blurred peaks. Due to that only TP films on PE and CuI were further analysed. Rocking curve measurements of both sample were performed (figure 6.15) which show that the molecules are not perfectly aligned in layers parallel to the surface.

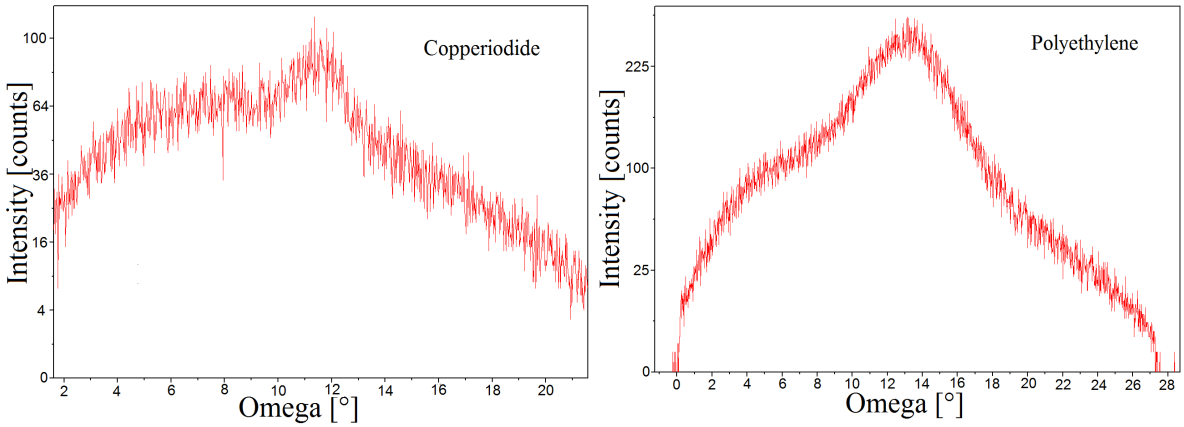

Figure 6.15: Rocking curve measurement at two selected peaks, namely the 004 reflection for TP on PE on the right and the 030 reflection for TP on CuI on the left. Both pictures show not well defined preferred orientation.

The samples were measured at HASYLAB and as good as possible indexed. A result was found were the same triclinic structure appeared on both substrates, lying molecules on CuI and upright standing molecules on PE. This phase is newly discovered for TP thin film samples. Despite the low crystallinity, the intensities of eight Bragg peaks were extracted although the allocation of correct intensities was not exact due to the wide and blurred peak shape. However the results of the FOX structure simulation allowed an educated guess of the molecular arrangement of this TP phase on two surfaces.

7 Phenylene-Butoxyphenyl-Acrylonitrile (DBDCS)

Park et al. experimented with luminescent molecular sheets of DBDCS which enable a two-colour florescence switching in response to pressure, temperature and solvent vapour. The cause of this multi-stimuli switching effect are C-H$\cdots$N and C-H$\cdots$O hydrogen bonds which form two distinctive DBDCS crystal phases, namely the B- and G-phase, by promoting shear-sliding and therefore significant changes in the dipole coupling. As a consequence the π-orbital overlap also changes. This interesting property lead to a rewritable fluorescent optical recording medium presented in [44].

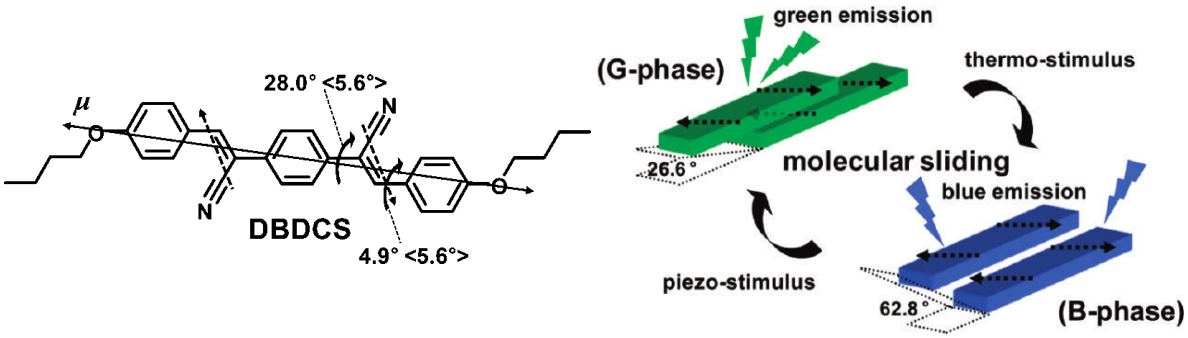

Figure 7.1: On the left the structural formula of DBDCS and on the right a schematic representation of the application in an optical recording medium. The dashed black arrows in both pictures indicate the dipoles moments which enable the property of switching. Both images taken from [44].

In order to understand the physical processes it is crucial to know the structure of the material. The G-phase is already solved but the B-phase is not fully explained. Task was to determine the structure of the DBDCS B-phase. The group around Johannes Gierschner manufactured B-phase thin film samples by means of vapour deposition on 100°C hot glass. The investigated samples had a film width of approximately 1μm.

7.1 Indexation

The GIXD measurement in figure 7.2 was performed at the HASYLAB W1 beamline and the indexation resulted in the lattice constants a = 9,851Å, b = 10,094Å, c = 27,455Å, α = 85,42°, β = 89,67° and γ = 85,91° with triclinic symmetry. Contact plane of the unit cell on the substrate is the (0 0 1) plane. The unit cell contains four DBDCS molecules and the respective density ρ of 1,17$\frac{g}{cm^3}$ is reasonable.

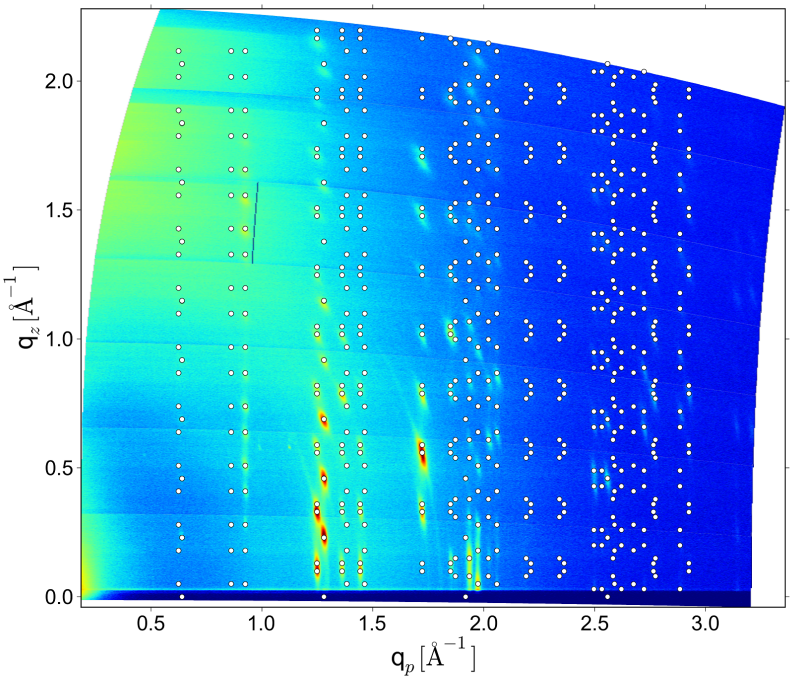

Figure 7.2: Indexation of the DBDCS thin film. The incident angle at the W1 beamline was 0,15°. In the experiment not all peaks are visible due to low intensity.

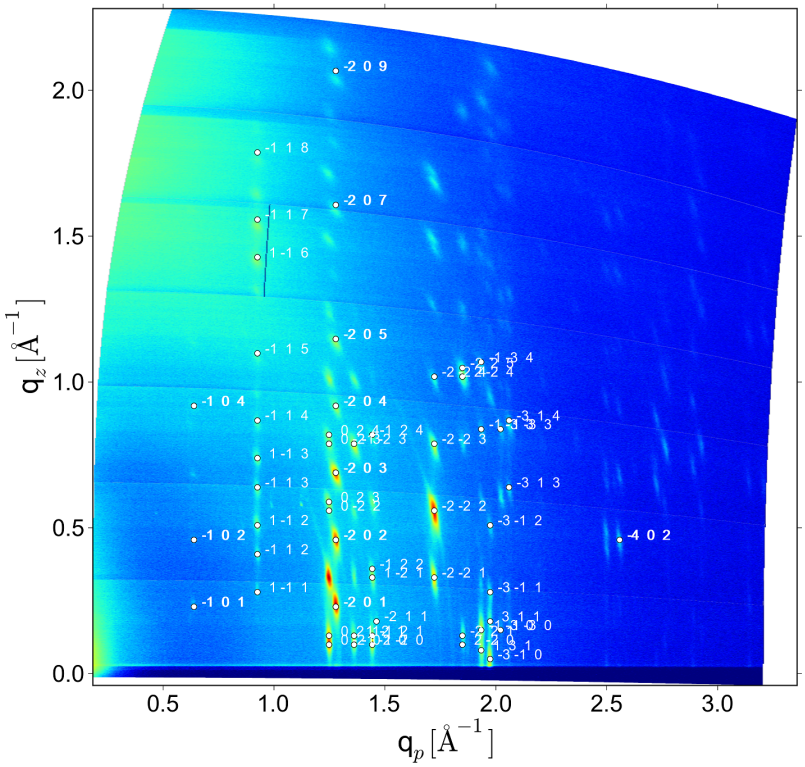

Figure 7.3: Extracted Bragg peaks for the FOX optimization.

7.2 Intensity Extraction

64 Bragg peaks were extracted as pictured in figure 7.3. The extraction of overlapping peaks is difficult since there is no clear assignment of the correct intensities to the respective peaks. The double peak data of the line scans was fitted in the software Fityk[47]. Moreover peaks between two maps can not be fitted due to different backgrounds on different maps.

7.3 Structure Simulation

The molecular conformation was taken from the DBDCS single crystal solution. The four molecules were fixed on the sites 0 0 0; 0,5 0 0; 0 0,5 0 and 0,5 0,5 0 in fractional coordinates of the unit cell. First the simulation did not show physically possible solutions. The molecules were entangled and intersected each other. To inhibit such behaviour during optimization a so-called anti-bump constraint was introduced. The anti-bump is as mentioned in appendix A an additional cost value to prevent the molecules getting too close. In order to get reasonable results this anti-bump cost had to be scaled high.

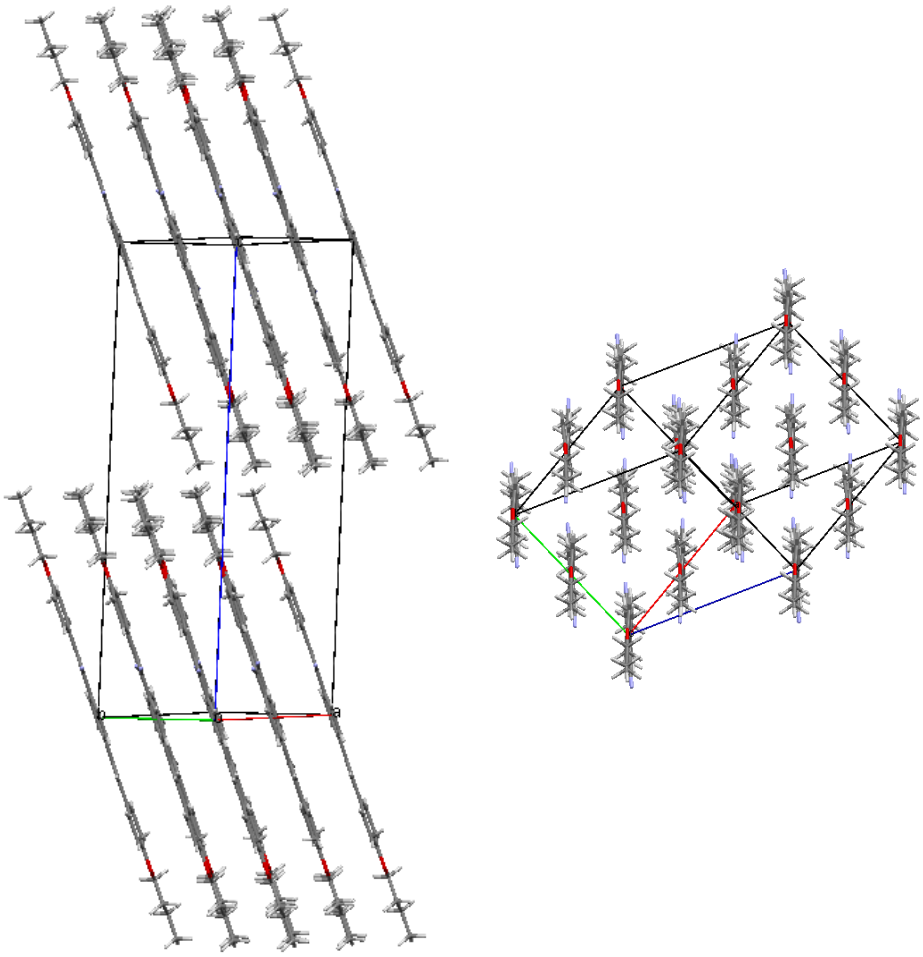

Figure 7.4: Sandwich structure for DBDCS B-phase with high scaled anti-bump cost.

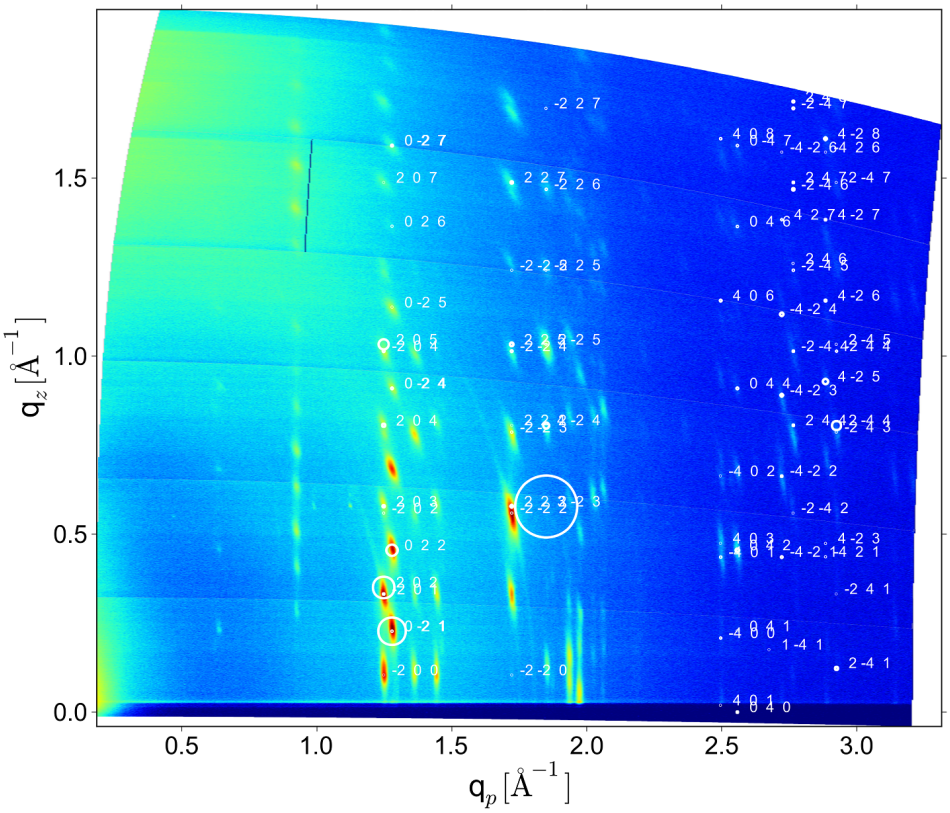

Figure 7.5: Reciprocal space map of the DBDCS thin film sample with calculated intensities (white circles). The structure solution does not fit.

The problem was to find a suitable scaling since too high multiplicands always lead to the same well defined sandwich structure as displayed in picture 7.4. The presented structure might be physically reasonable but it does not match the measured GIXD pattern in figure 7.5.

The reciprocal space map of the best result obtained in various simulation runs with varying scaling for the anti-bump cost as well as different positions of the four molecules is shown in figure 7.6 and 7.7. In this simulation the anti-bump cost was scaled with 1500 and additionally one peak was artificially set to zero. However setting peaks zero does manipulate the scattering data and does not always lead to better results. In particular the above mentioned result was not the structure with the lowest cost value in the FOX simulation but it was the best solution which is physically feasible, i.e. there are no touching atoms. One problem is that it is not possible to work with partially rigid molecules, e.g. to allow the side chains of DBDCS to be flexible. However, the major drawback for the structural simulation of DBDCS is the complexity of the system combined with the little amount of data from the GIXD experiment.

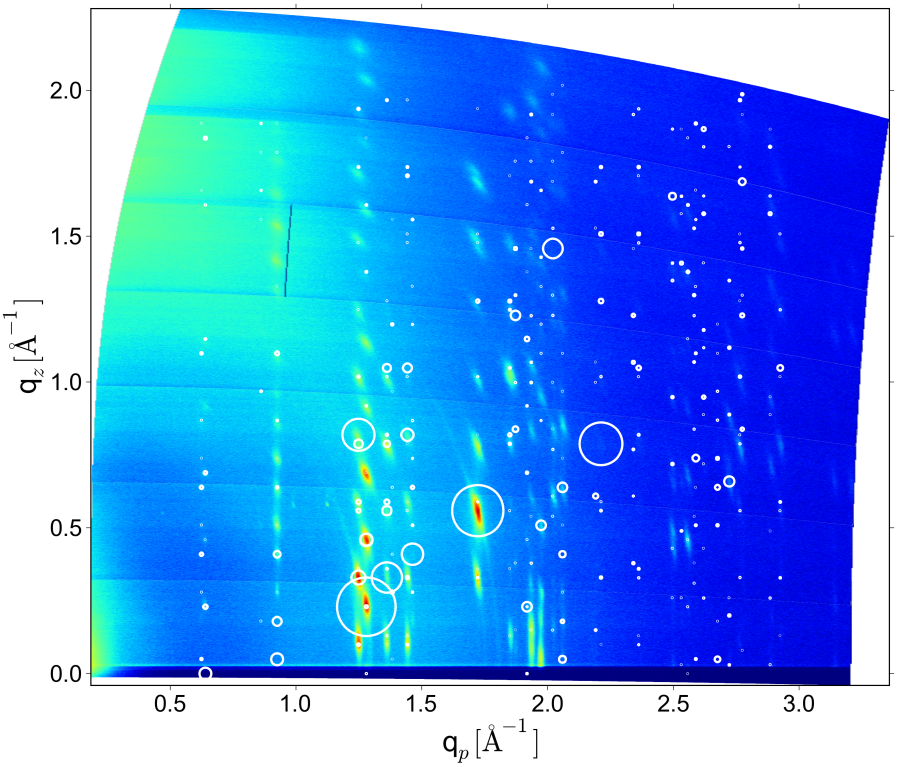

Figure 7.6: Reciprocal space map of the DBDCS thin film sample with calculated intensities (white circles). The calculated intensities arising from the structure solution do fit to some extend.

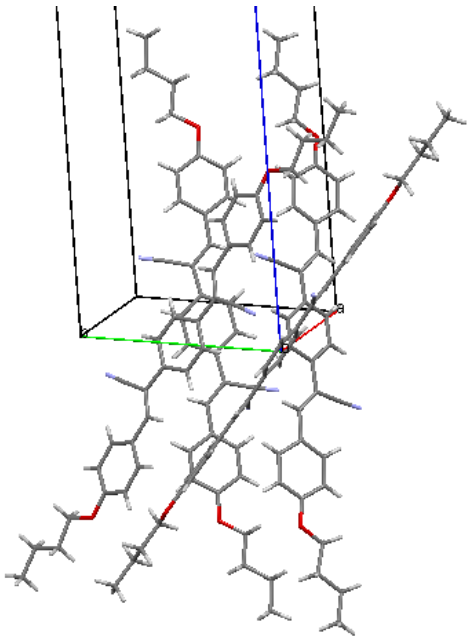

Figure 7.7: Molecular arrangement of the four molecules in the unit cell for the simulation with the reciprocal space map in figure 7.6.

7.4 Conclusion

The DBDCS B-phase was indexed from a GIXD measurement conducted at HASYLAB. The found triclinic unit cell explains all measured Bragg peaks. Structure optimization in FOX did not lead to a satisfying result. This might have multiple reasons: First the structure has low symmetry and four molecules in the unit cell which make the problem rather complex. An other issue was the extraction of the overlapping intensities and peaks between two measured reciprocal space maps, i.e. it was not possible to assign correct intensities. Furthermore the in fact flexible side chains of DBDCS (see figure 7.1) were assumed to be rigid which is physically not reasonable. Side chains have a huge impact on the solid-state packing of conjugated oligomers[6].

During the simulations in order to get reasonable structures, constrains had to be added which of course restricted the outcome of the optimization. Sandwich structures were only obtained under strong constraints and other physically feasible structures were not reproducible. Therefore no satisfying result was achieved. In a next step a different approach by applying molecular dynamical methods is considered.

Part IV

Conlusion

Summary and Conclusion

The general procedure for a structure resolution from a crystalline thin film sample starts with the precharacterisation of the sample at a GIXD adapted Bruker D8 diffractometer in the home laboratory. Additionally AFM scans and specular X-ray scans can be informative about the orientation of the molecules or about the presence of multiple phases. The actual measurement is in general conducted at a synchrotron facility. In this work all necessary GIXD measurements were done at beamline W1 at HASYLAB in Hamburg. The analysis of the obtained reciprocal space maps in PyGid lead to unit cell parameters and crystal symmetry of the respective material. With this information and the extracted intensities of the Bragg peaks a structure simulation was done in the software FOX. The results had to be interpreted and evaluated with respect to the laws of physics. In the next step either constrains had to be introduced or reasonable results had to be validated by multiple reruns yielding the same molecular arrangement.

The molecule dioctylbenzothieno-benzothiophene (C8 BTBT) is heavily studied and therefore the crystal structure was already resolved and published in 2008. So for this work the molecular structure was a test case in order to learn something about the accuracy of the structure-resolution-via-GIXD approach. However the C8 BTBT thin film was not of good enough quality, i.e. the Bragg reflections were blurred and not extractable. To perform a structure resolution through simulation was therefore not possible. This film was prepared by spin coating which emphasises that spin coated films are usually of lower quality than epitaxially grown films e.g. with hot wall epitaxy grown thin films. Nevertheless an indexation was feasible and the found unit cell values are in good accordance to the literature values.

The organic molecule ternaphtalene (NNN) packs in an unknown structure. Samples on two different substrates were examined. The sample on SiO_2 showed well defined diffraction features which alleviated the indexation and extraction of the Bragg peaks. The FOX simulation yielded in a reproducible herringbone structure which is indicated for molecules like NNN. Due to the low amount of reflections (60), the uncertainty of the intensity extraction as well as the uncertainty for the GIXD measurement and the fixed planar conformation of the NNN molecule, the obtained standard residual factors (R and wR) for this structure resolution are not satisfactory. However it is important to point out that those factors were established for 3-D powder diffraction. Due to the thickness of the film sample the resolved structure is the bulk phase of NNN which is proven by X-ray powder diffraction. This enabled a Rietveld analysis of the NNN powder which yielded in slightly different lattice constants. Nevertheless satisfactory residual factors were also not achieved for the Rietveld refined NNN structure.
It was possible to explain most of the measured Bragg reflections for the NNN thin film on HOPG with the found bulk phase indexation. Next to lying molecules, where the molecular backbones are parallel to the surface, standing molecules are present which is in accordance to the AFM measurement.

Dibromo-indigo widely know as Tyrian purple (TP) is a famous dye which is in the focus of science due to its optical and electrical properties. First measurements at the epitaxial grown film revealed that the known bulk phase is present. Despite this

a structure resolution with the in this work presented approach was performed and resulted in a crystal structure which is in good accordance to the published molecular packing of TP.
Two spin coated thin film samples on polyethylene (PE) and on copper-iodide (CuI) respectively showed a surface induced effect. It appears that the same triclinic TP thin film phase is present on both surfaces with standing molecules on PE and lying molecules on CuI. The low crystallinity of the samples inhibited a structure resolution as for the bulk phase. However the conducted simulations gave an idea about the molecular orientation. The experiment approved the expected molecular alignment on the surface but could not give accurate results about the crystal structure.

Phenylene-butoxyphenyl-acrylonitrile (DBDCS) exhibits at least two stable phases whereas the so-called B-phase of DBDCS was not resolved but the above introduced procedure was applied and matching lattice parameters were obtained. However a satisfying structure solution was not found. The reasons are firstly the issue with the intensity extraction (overlapping peaks and peaks between reciprocal space maps) and secondly problems which result from the complexity of the problem (triclinic unit cell with 4 molecules in the basis). Moreover the limitation of a rigid molecule in which the flexibility of the side chains is not considered is another issue. Nevertheless the rigid body assumption and the anti-bump constraint, which prevented that the molecules get too close or even intersect, had to be introduced in order to generate physically reasonable structures. Thereby the scaling of the anti-bump cost was difficult since high scales restrict the system in a way that it always produces the same result. Low scaling on the other hand is not strong enough to inhibit intersection of molecules.

Appendix

FOX Manual

This is just a brief manual of a crystal structure solution procedure in the software Free Objects for Crystallography, abbreviated with FOX. Comprehensive software documentation and tutorials can be found in the FOX wiki[48].

To start an ab initio crystal structure simulation in FOX first one has to insert a new crystal (menu Objects - New crystal). In the appearing graphical user interface (GUI) in figure 8 the unit cell parameters, symmetry and the molecule are inserted. The

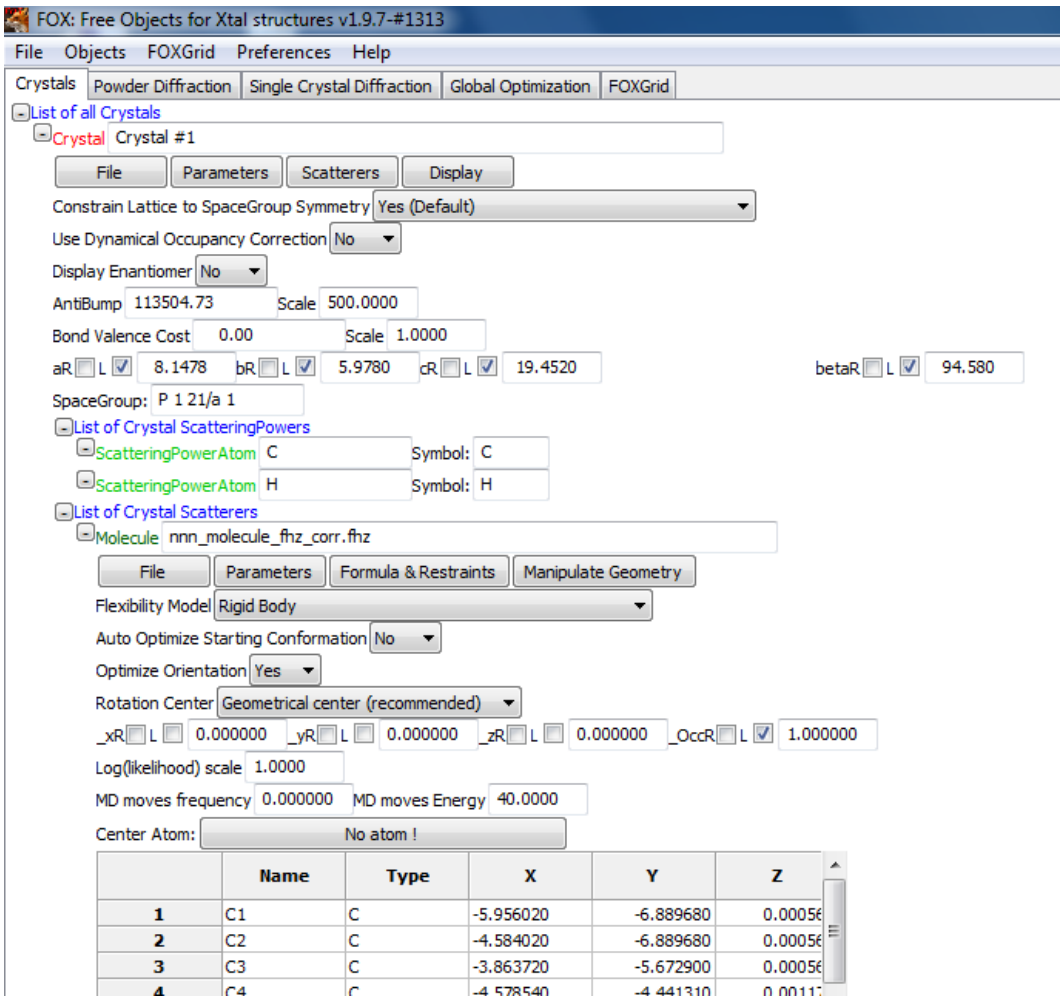

Figure 8: Graphical user interface (GUI) of FOX to insert the crystal data.

molecule is inserted as Fenske-Hall Z matrix. In order to get such a representation of the molecule, all atom kinds (e.g. carbon C, hydrogen H, etc.) are inserted as scatterers (Scatterers - Add Atomic Scattering Power) and from that the molecule is build (Scatterers - Add atom) and merged (Scatterers - Convert Atoms to a Molecule). Depending on the kind of the coordinates, e.g. fractional or Cartesian, the correct positions have to be inserted either before merging or after merging the atoms. Atoms or whole molecules are displayed in fractional coordinates of the unit cell however atoms of a molecule are represented by Cartesian coordinates. Bond restraints have to be added for the atoms of the molecule (Formula & Restraints - Add Bond Restraint).

The obtained molecular structure is exported as Fenske-Hall Z matrix (Molecule options - File - Export to Fenske-Hall Z matrix). This command creates an output file in the correct shape which can be reloaded anytime. Troubles, i.e. the molecule is not rebuild correctly when imported, may arise from the order of the atoms in the list which represents the molecule. This might be circumvented by changing the order (has to be done before merging to a molecule) or artificially correcting the coordinates of the affected atoms.
For GIXD data it is advisable to set the molecule rigid and therefore no optimization of the starting conformation is required. In fact due to the low number of diffraction features rigid body refinement is the only reasonable way for solving crystal structure for thin films of organic molecules from GIXD data[28]. The software then optimizes the orientation of the molecules in real space. The user merely has to assign positions for the molecules in the unit cell, if symmetry conditions do not directly results in a proper occupation of the unit cell. The ticks in front of the respective x, y, z values indicate if those positions are open for optimization. In order to achieve convergence it is usually better to fix the molecular positions for GIXD data. FOX displays the actual molecular orientations in real space (button Display) even during simulation runs.
In order to activate the anti-bump constraint the van der Waals distances between the atoms in the respective table (Scatterers - Show Scattering Powers Parameters Window - AntiBump) have to be set and the anti-bump cost has to be scaled in the "Crystals" window.

In the next step a single crystal diffraction object (Objects - New Single Crystal Diffraction) is added. The GUI window is displayed in figure 9. The important inputs on this

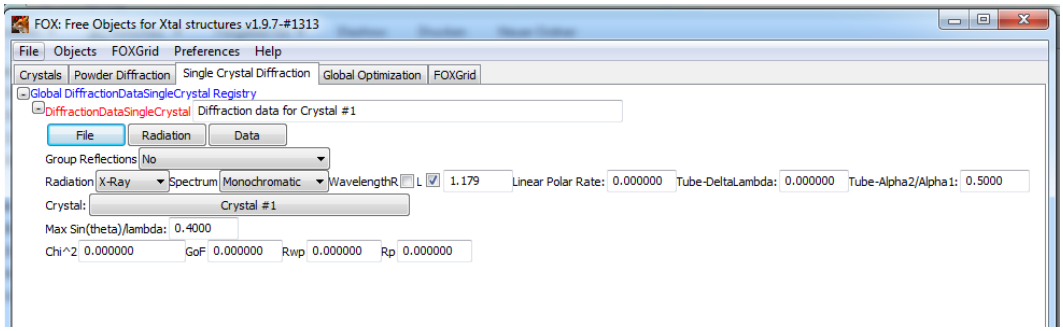

Figure 9: Graphical user interface (GUI) of the Single Crystal Diffraction object.

page are the experimental setup dependent wavelength and the obtained extracted and corrected structure factor of the observed Bragg peaks of the reciprocal space map. The input file is already generated by an other script (correct_iobs.py, see section 3.3.1) and is just imported in this window (File - Import HKL Iobs). Multiple peaks on the same position are considered by multiple entries in the input file. Such files are loaded into FOX with the option "Import Reflections with group intensity". The command "Data - Show Graph" displays the measured structure factors and the structure factors of the structure which is currently simulated. The lower boxes display the current χ^2-value as well as the residual factors as introduced in section 2.2.5.

In order to start the simulation an other object for the optimization has to be inserted (Objects - New Monte Carlo Object). In this window (figure 10) input for the opti-

mization is given and the relevant objects for the simulation are loaded (Optimized Objects - Add object to optimize). The crystal and the respective crystal diffraction data has to be added. Then the optimization settings can be inserted and the simulation started. The algorithm then alters the molecular orientation in real space and χ-minimizes the respective calculated structure factors F_{calc} with the measured input values from the experiment F_{obs} according to

$$\chi^2 = \sum_i \frac{||F_{obs,i}|^2 - |F_{calc,i}|^2|}{\sigma^2_{F_{obs,i}}}. \quad (1)$$

Whereas $\sigma_{Fobs,i}$ is the standard derivation of the observed structure factors.

The obtained solutions can be checked in FOX or the resulting crystal can be exported as cif-file.

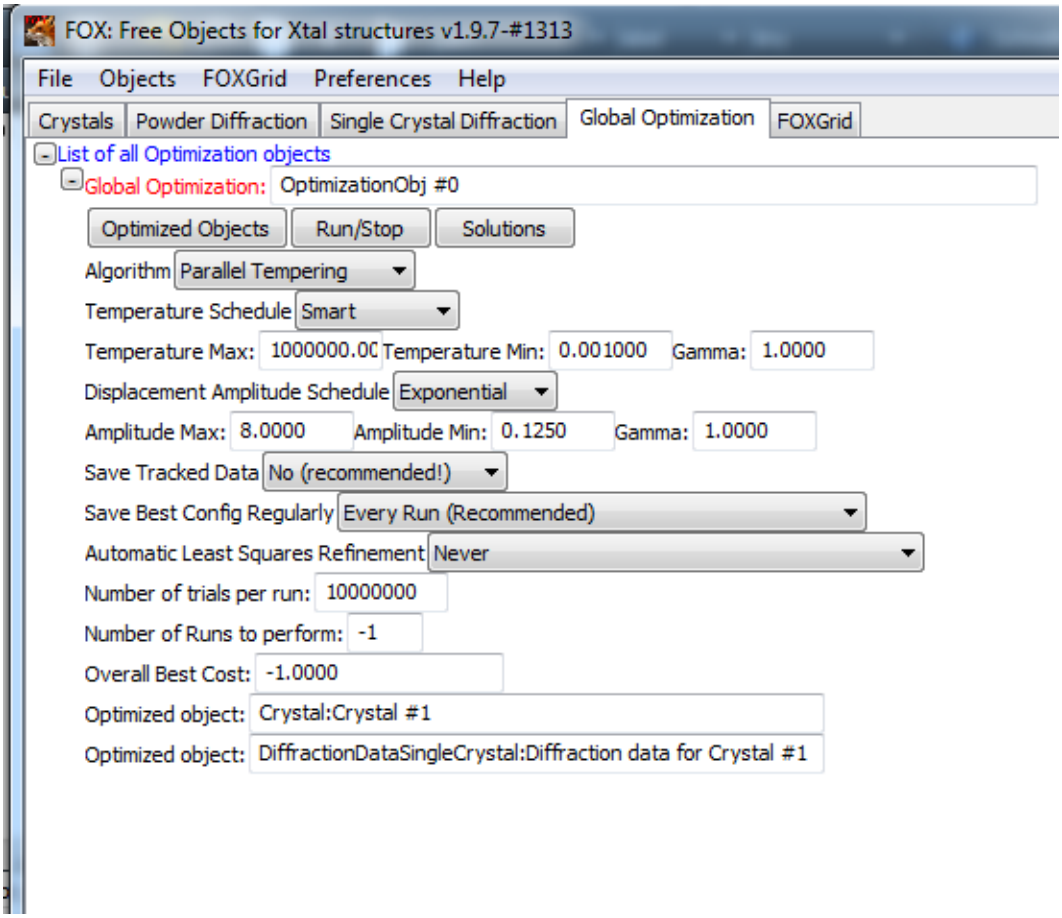

Figure 10: Graphical user interface (GUI) of the optimization object.

Bibliography

[1] Mihai Irimia-Vladu et al.; Environmentally sustainable organic field effect transistors, 2010, Organic Electronics, Elsevier

[2] Vainshtein, Fridkin, Indenbom; Structure of Crystals, edition 2, 1995, Sringer-Verlag

[3] A.I. Kitaigorodsky; Molecular Crystals and Molecules, 1973, Academic Press

[4] C.P. Brock and J.D. Dunitz; Towards a Grammar of Crystal Packing, 1994, Chem. Matter, 6, 1118-1127

[5] W. Brütting; Physics of Organic Semiconductors, 2005, Wiley-VCH

[6] M.D. Curtis et al.; Solid-State Packing of Conjugated Oligomers: From π-Stacks to Herringbone Structure, 2004, JACS articles

[7] D. E. Williams, Y. Xiao; Benzene, Naphthalene and Anthracene Dimers and their Relation to the Observed Crystal Structures, 1992, Acta Cryst. A 49, 1-10

[8] G.R. Desiraju and A. Gavezzotti; Crystal Structures of Polynuclear Aromatic Hydrocarbons. Classification, Rationalization and Prediction from Molecular Structure, 1989, Acta Cryst. B45, 473-482

[9] R.Fachioni and G. Grosso; Organic Electronic Materials, 2001, Springer Series in Material Science

[10] A. Winkler; Article *"Thermal Desorption of Organic Molecules"* in Interface Controlled Thin Films, Springer Proceedings in Physic 129, 2009

[11] I. Salzmann, A. Moser et al.; Structure Solution of the 6,13-Pentacenequinone Surface-Induced Polymorph by Combining X-Ray Diffraction Reciprocal-Space Mapping and Theoretical Structure Modeling, 2011, Crystal Growth & Design, Vol. 11, 600-606

[12] A. Saleo, R.J. Kline, D.M. Delongchamp, M.L. Chabinyc; Microstructural Characterisation and Charge Transport in Thin-Film Transistors, Advanced Materials, 2010, 22, 3812

[13] B. Servet, G. Horowitz, S. Ries, O. Lagorsse, P. Alnot, A. Yassar, F. Deloffre, P. Srivastava, R. Hajlaoui, P. LAng, F. Garnier; Polymorphism and Charge Transport in Vacuum-Evaporated Sexithiophene Films, Chem. Mat. 6, 1994, 1809

[14] J. Fraxedas, J. Caro, J. Santiso, A. Figueras, P. Gorostiza, F. Sanz; Polymorphic transformations observed on molecular organic thin films: p-nitrophenyl nitronyl nitroxide radical, Europhys. Lett. 48, 1999, 461

[15] R. Resel, N. Koch, F. Meghdadi, G. Leising, L. Athouel, G. Froyer, F. Hofer; A Polymorph Crystal Structure of Hexaphenyl Observed in Thin Films, Cryst. Res. Technol. 36, 2001, 47

[16] H. Muguruma, T.K. Saito, S. Hotta; Conformational polymorphs in vacuum evaporated thin films of 5,5"bis[(2,2,5,5-tetramethyl-1-aza-2,5-disila-1-cyclopentyl)ethyl]-2,2':5',2":5",2"'-quaterthiophene, Thin Solid Films 445, 2003, 26

[17] I. Salzmann, S. Duhm, G.Heimel, J:P: Rabe, N. Koch, M. Oehzelt, Y. Sakamoto and T. Suzuki; Structural Order in Perfluropentacene Thin Films and Heterostructures with Pentacene, Langumir 24, 2008, 7294

[18] S. Kowarik, A. Gerlach, S. Sellner, L. Cavalcanti, F. Schreiber; Real-time X-ray diffraction measurements of structural dynamics and polymorphism in diindenoperylene growth, Appl. Phys. A 95, 2009, 233

[19] Young Hee Park et al.; Ab initio Studies on Acene Tetramers: Herringbone Structure, 2007, Bull. Korean Chem. Soc. Vol. 28, No. 8

[20] M. Birkholz; Thin Film Analysis by X-Ray Scattering, 2005, Wiley-VCH

[21] Ch. Kittel; Einführung in die Festkörperphysik, edition 14, 2005, Oldenburg

[22] D. Schwarzenbach; Kristallographie, Springer Verlag

[23] http://en.wikipedia.org/wiki/File:BraggPlaneDiffraction.svg, date 10.05.2013

[24] http://en.wikipedia.org/wiki/File:Ewald_Sphere.svg, date 10.05.2013

[25] S. Stepanov, Grazing-incidence X-Ray Diffraction, Illinios Institute of Technology

[26] M. Neuschitzer; Diploma thesis: Grazing incidence in-plane X-ray diffraction on ultra-thin organic films using standard laboratory, 2012, Techn. Univ. Graz equipment

[27] M. Neuschitzer, A. Moser, R. Resel et al; Grazing-incidence in-plane X-ray diffraction on ultra-thin organic films using standard laboratory equipment, 2012, Journal of Applied Crystallography

[28] A. Moser; PhD thesis: Crystal Structure Determination from Two-Dimensional Powders, 2012, Techn. Univ. Graz

[29] L. Spieß, R. Schwarzer, H. Behnken, G. Teichert; Moderne Röngtenbeugung, 2005, Teubner

[30] D.B. Bennet; Understanding Single-Crystal X-Ray Crystallography, 2010, Wiley-VCH

[31] R.A. Young (editor); The Rietveld Method, 1993, Oxford Univ. Press

[32] P. Müller et al.; Crystal Structure Refinement - A Crystallographer's Guide to SHELXL, 2006, Oxford Univ. Press

[33] Favre-Nicolin, V. and Cerny, R. (2002). FOX, "free objects for crystallography": a modular approach to ab initio structure determination from powder diffraction, Journal of Applied Crystallography 35(6)

[34] Liu Chuan, Minari Takeo, Lu Xubing, Kumatani Akichika, Takimiya Kazuo, Tsukagoshi Kazuhito; Solution-Processable Organic Single Crystals with Bandlike Transport in Field-Effect Transistors, Adv Mater 2010

[35] Izawa Takafumi et al.; Molecular Ordering of High-Performance Soluble Molecular Semiconductors and Re-evaluation of Their Field-Effect Transistor Characteristics, Advanced Mater, 2008

[36] Applied Physics Express 2010, 3, 121601

[37] P.Busch, M. Rauscher et al.; Grazing-incidence small-angle X-ray scattering from thin polymer films with lamellar structures - the scattering cross section in the distorted-wave Born approximation, 2006, J. Appl. Crystallography

[38] M. Rauscher et al.; Grazing incidence small angle x-ray scattering from freestanding nanostructures, 1999, J. Appl. Phys. 86, 6763

[39] I.K. Robinson et al.; Rep. Prog. Phys., 1992

[40] M.P. Tate et al.; Simulation and Interpretation of 2D Diffraction Patterns from Self-Assembled Films at Arbitrary Angles of Incidence: From Grazing Incidence (Above the Critical Angle) to Transmission Perpendicular to the Substrate, 2006, J. Phys. Chem. B

[41] E.D. Glowacki et al.; Indigo and Tyrian Purple – From Ancient Natural Dyes to Modern Organic Semiconductors, 2012, Israel Journal of Chemistry

[42] Naturwissenschaften (1979), 66, 110

[43] Acta Chem.Scand.A (1980), 34, 171

[44] S.J. Yoon, J. Gierschner, S.Y. Park, et al.; Multistimuli Two-Color Luminescence Switching via Different Slip-Stacking of Highly Fluorescent Molecular Sheets, 2010, JACS articles

[45] http://www.ccdc.cam.ac.uk/Solutions/CSDSystem/Pages/Mercury.aspx

[46] http://www.gaussian.com/

[47] http://fityk.nieto.pl/

[48] http://vincefn.net/Fox/FoxWiki